Anomalous Phenomena and Spectral Tailoring in Photonic Crystals

by

Michael Ghebrebrhan

Submitted to the Department of Physics
in partial fulfillment of the requirements for the degree of

Doctor of Philosophy

at the

MASSACHUSETTS INSTITUTE OF TECHNOLOGY

September 2010

Author .....
Department of Physics
August 15, 2010

Certified by .....
John D. Joannopoulos
Francis Wright Davis Professor of Physics
Thesis Supervisor

Accepted by .....
Krishna Rajagopal
Associate Department Head for Education

Anomalous Phenomena and Spectral Tailoring in Photonic Crystals

by

Michael Ghebrebrhan

Submitted to the Department of Physics
on August 15, 2010, in partial fulfillment of the
requirements for the degree of
Doctor of Philosophy

Abstract

Photonic crystals are recently discovered meta-materials whose optical properties arise from periodic refractive index variations. In this thesis I examine various aspects of photonic crystals including a self-assembled photonic crystal, anomalous properties arising from periodicity, and tailoring absorption and emission spectra. Fabricating photonic crystals with the desired properties in the infrared and optical frequencies, including a complete photonic bandgap, is an experimental challenge. Self-assembly can provide a solution. In Chapter 2, I examine a new type of colloidal photonic crystal of tetrahedral building blocks in a fcc lattice that is found to possess a robust and complete bandgap. In Chapter 3, I explore the photonic states that exist around a zero-group velocity point. Motivated by negative refraction, a measure of the effective wavevector is constructed that distinguishes various types of zero-group velocity modes. Around one type of zero-group velocity mode, an anomalous region of backward effective wavevector is found that enables superior light confining properties of a mirror-less cavity. In the last two chapters I look at the problem of efficiently converting radiant energy to electrical power. In Chapter 4, I explore the extent to which 1D multi-layer thin films can enhance the short circuit current of a 2 μm-thick silicon solar cell. Though such cells are limited by their size, for two front-layers a relative boost of 45% is possible. Finally, in Chapter 5, motivated by the problem of low efficiency in thermophotovoltaics, I look at selective emissivity of a 2D metallic photonic crystal. A semi-analytical theory is developed using only the material dispersion and geometrical parameters. Applications of the selective emitter, including power generation and lighting, are discussed.

Thesis Supervisor: John D. Joannopoulos
Title: Francis Wright Davis Professor of Physics

Acknowledgments

This thesis would not be possible without the support and guidance of those around me. Over the years I spent here at MIT, I've been fortunate to gain much from people who've help me grow as a scientist and as a person. First I want to thank my advisor John Joannopoulos for his generous patience, guidance, and support during the course of my Ph.D. I was pretty lucky to work on photonics at this exciting time when there so many opportunities, and John is second to none when it comes to passing on this enthusiasm. I also wish to thank professors Steven Johnson and Marin Soljačić for sharing their amazing physical insight. Finally I wish to thank my thesis committee, John, Marin, and professor David Litster, for taking the time to read this thesis and sit on the committee.

There are many within the JDJ/SGJ/MS group that took out time for me and shared their knowledge. My 12-111 officemates, Peter Bermel and David Chan, helped me get started with the different software our group used. Peter especially has always been willing to help– whether it was problems with Debian, the supercomputers, or some physics question. Mihai Ibanescu's guidance during my early years cannot go unrecognized, sharing an interesting paper he found or taking time for my questions. My neighbors in the new CMT building, Aristos Karalis and Alejandro Rodriguez, always had time for enlightening discussion. Karen Lee was a great officemate to have. Ivan Celanovic, who worked closely with the group, made the selective emitter project fun. Finally to the rest of the group, I extend my thanks!

Outside of the JDJ group, Mark Rudner stands out. He is a great friend and amazing colleague, a combination not easily found. Mark keeps it real. The 8.333-8.511 homework group composed of Mark, Steve Jordan, Seungeun Oh, Pouyan Ghaemi, Rich Ott, and myself was a source of friendship since the very first week I

started here. Lastly the Black Graduate Students Association was always a source of camaraderie.

My time here was greatly enhanced by the community I found outside of MIT. A special thanks belongs to Habtom Ghiorgis for both his friendship and introducing me to the Eritrean community here. They have been like a second family. In particular, Musie Ghebremichael and Aman Russom have been like older brothers, who always had advice and served as sources of inspiration.

I've been most fortunate to have Rays Jiang in my life. Her presence, spirit, and intellect rejuvenates and inspires me.

Finally and most importantly, I wish to acknowledge the unending love and support from my parents and sister, who've made this possible. I remember the very first science book my parents bought for me when I was a small child; I had no idea where it would eventually take me. The weekends and summers I spent working with my dad laid the foundation for everything I do now. A well-timed phone call from my parents would revitalize me and quickly erase doubts and frustrations. It is their love that drives me forward.

Contents

1 Introduction **15**

1.1 The photonic crystal in detail 16

1.2 Thesis overview 18

2 Tetrastack: colloidal photonic crystal **25**

2.1 Introduction 26

2.2 Tetrastack 27

2.3 Fabrication of tetrastack 32

3 Distinguishing zero-group velocity modes in photonic crystals **35**

3.1 Introduction 35

3.2 $\eta_{\mathbf{H}}$ in 1D photonic crystals 38

3.3 $\eta_{\mathbf{H}}$ in 2D photonic crystals 40

3.4 Mirrorless cavity 46

4 Optimization of front coatings **54**

4.1 Introduction 54

4.2 Formulation of the problem 56

4.3 Results and discussion 62

4.4 Conclusions and future work 75

5 Tailoring thermal emission via Q-matching of photonic crystal resonances **78**

5.1 Introduction 78

5.2 Loss rates of waveguide resonances 80

5.3 Effect of period 84

5.4 Coupled-mode theory 88

5.5 Applications and conclusions 93

6 Conclusion **96**

List of Figures

1-1 From left to right, one-, two-, and three-dimensional photonic crystals. Red and blue denote regions of low and high index. 16

1-2 Band structure of a three-dimensional photonic crystal. The photonic bandgap is highlighted yellow. 19

1-3 Photon number flux per unit wavelength of two blackbody emitters, one at 5600 K (blue) and another at 1000 K (red). The spectrum of the cooler emitter has been rescaled by 100. Shaded regions denote useful photons for a silicon (blue) and InGaAsSb (red) PV diode. . . 22

2-1 (a) SEM images of fabricated tetrahedral colloidal particles. (b) Tetrastack particles at the lattice points of the photonic crystal. (c) Conventional unit cell of diamond photonic crystal. 26

2-2 Band structure of inverted tetrastack in silicon ($n_c = 3.4$) with sphere radius $0.27a$. Inset, a portion of the tetrastack photonic crystal unit cell. 28

2-3 Bandgap map of ZnS-air ($n_c = 2.29$) and Si-air ($n_c = 3.4$) colloidal structures. 31

2-4 Relative bandgap size versus index constrast for various structures at filling fractions corresponding to optimal relative bandgaps. 32

2-5 Rotating the tetrastack particles away from the unit cell main diagonal (111) to a face diagonal (110) reduces the size of the bandgap. 33

3-1 Typical 1D band structure for a Bragg mirror with high dielectric $\varepsilon = 9$ and width $d = 0.2a$ 37

3-2 (a) $\eta_{\mathbf{H}}$ calculated across the 1st and 2nd bands. (b) The magnitudes of the dominant Fourier components across the second band of Fig. 3-1. Away from the band edges, where strong mixing occurs, the second band behaves as a plane wave with $ka/2\pi \rightarrow ka/2\pi - 1$. 39

3-3 2D band structure with dielectric profile (inset) $\varepsilon = 9$, $r = 0.2a$. Circled are the different types of zero-group velocity points; labels indicate location in the irreducible Brillouin zone and band number. . 41

3-4 $\eta_{\mathbf{H}}$ for the first four bands of the two-dimensional crystal in Fig. 3-3. 42

3-5 (a) $\mathbf{k}+\mathbf{G}$ associated with the largest Fourier components for the second band, and magnitudes of associated Fourier components across the same band. (b) $\mathbf{k} + \mathbf{G}$ for third band, and magnitudes of associated Fourier components across the band. 44

3-6 (a) Plot of η (thin lines) and $\widetilde{\eta}$ (thick lines) for the second band. Color indicates the field used as the weight: $\mathbf{H}$ (blue) and $\mathbf{D}$ (red). (b) Same comparison but for the third band where behavior is expected to be normal. 45

3-7 Photonic-crystal Fabry-Perot cavity, formed by a finite number of layers of the crystal in the (11) direction. Here, the thickness is $L = 12d$, where $d = a/\sqrt{2}$ is the distance from one row of rods to the next. Blue/white/red indicate positive/zero/negative E_z field of a resonant mode with $Q \sim 2000$. 47

3-8 Resonant modes of a cavity formed from an finite section of a photonic crystal. The units of length is $d = a/\sqrt{2}$ where a is the lattice constant. The dashed gray lines mark the induced periodicity due to the k point with zero-group velocity. For (a) $\mathbf{k}a/2\pi = (0.293, 0.293)$ at $\Sigma 2$, (b) $\mathbf{k}a/2\pi = (0.5, 0.5)$ at M1 & M2 and (c) $\mathbf{k}a/2\pi = (0.318, 0.318)$ at $\Sigma 4$. 49

3-9 The second band minimum is shifted to $\mathbf{k}a/2\pi = (0.33, 0.33)$, which yields the same oscillatory dependence on L seen in the fourth band in Fig. 3-8(c). 50

3-10 Differences in the number of excited modes (circles) for the two cases in Figs. 3-8(a) and 3-8(b). 52

4-1 Schematic illustration of solar cell designs studied here: (a) a photovoltaically active silicon region (green), backed by a perfectly reflecting metal (gray), (b) diagram (a) with one or more front coating depicted in shades of blue, and (c) diagram (b) with one back dielectric coating layer. 57

4-2 Fits of calculation parameters (red curves) to actual data derived from references (blue curves): (a) real index of crystalline silicon [1] (b) absorption length of crystalline silicon [1] (c) current weights $w(\lambda)$ in Eq. (4.1), fit with a degree-100 Chebyshev approximation [2]. 59

4-3 A contour plot of the FOM of a cell with two front-coating layers versus the layer thicknesses (the indices of each layer are fixed at 1.27 and 4.35). The FOM ranges from 0.30 (blue) to 0.38 (red). The presence of many local optima necessitates a global optimization approach. . 60

4-4 The generated current efficiency as a function of wavelength; the parameters for each structure class (e.g., two front layers) are optimized separately at each wavelength i.e., this is the reflection spectrum for many different structures. Note that structures with one or more front layers display full absorption up to a particular wavelength λ_t that increases with the number of front layers. 63

4-5 The absorptive Q (magenta) and the radiative Q of 1,2, and 3 front coatings versus wavelength. Below 550 nm Q-matching is unnecessary, since the absorption length is equal to or less than the silicon layer thickness, and absorption is due to an anti-reflection coating. 65

4-6 The generated current efficiency versus the bandwidth of incoming radiation; for bandwidths up to 265 nm the central wavelength is 902.8 nm, for bandwidths above 265 nm, the maximum wavelength is fixed, while the minimum wavelength is decreased (which corresponds to a blue shift of the central wavelength). 68

4-7 Absorption spectrum over the full absorbing bandwidth for a thin-film crystalline silicon solar cell ($t = 2\mu$m). (a) Optimized over the full bandwidth and (b) optimized only at $\lambda = 902.8$ nm. 69

4-8 Figure of merit versus silicon slab thickness, both for a structure with no front layer (based on Fig. 4-1(a)) and optimized structures with 1-3 front layers (based on Fig. 4-1(b)). 71

4-9 Relative difference in figure of merit, calculated as the relative difference of the FOM for the optimized structure with the given reflection phase and the FOM of a structure with the given phase and with the optimized front coating of the reference phase ($\theta = 0$), versus the Fresnel reflection amplitude phase of the silicon-metal boundary. . . . 73

4-10 Absorption spectrum of the optimized single front coating reference structure for two different back-reflector phases, $\pi/4$ (blue) and π (red). The back-reflector simply shifts the peaks, but has a only negligible effect on the integrated absorption or the FOM. 74

5-1 Emissivity spectrum of flat, bulk tungsten (blue) and of an ideal selective emitter (green) designed to match the 0.6 eV/$\hbar$ bandgap of InGaAs. 80

5-2 A periodic array of cylindrical holes with period a, depth d, and radius R etched into a slab of tungsten. The hole depth is less than the tungsten slab thickness. 81

5-3 (a) Resonant mode frequency in units of $2\pi c/a$ with $a = 1$ μm, (b) Q_{abs}, and (c) Q_{rad} of the lowest three modes. The absorptive and radiative Q are plotted on the same color scale. Q-matching of the first resonance is indicated by the white line. 83

5-4 Q_{rad} versus period of unit cell with $R = 0.545\mu$m and $d = 1.89\mu$m. Resonance with a diffracted plane wave sets up an anti-crossing, visible as large jumps in Q_{rad}. Since we consider resonances that couple only to normal incidence, the period is bounded from above. 85

5-5 Absorption spectrum for the tungsten photonic crystal slab with $a = 4.8\,\mu$m, $R = 0.104a$, and $d = 0.394a$. Diffraction appears as sharp peaks and weak resonant peaks due to photonic crystal modes appear at approximately 2.7 and 3.4 $2\pi c/a$. 87

5-6 Absorption spectra for photonic crystal slabs with various a but R and d fixed at 0.5 and 1.89 μm, respectively. 89

5-7 A multimode resonator with resonant frequencies ω_i, absorptive and radiative lifetimes $\tau_{\text{abs},i}$ and $\tau_{\text{rad},i}$, respectively. Resonances i and j radiatively couple to each other with rate $1/\tau_{ij}$. 90

5-8 Absorptivity spectrum for $a = 1.2\,\mu$m calculated by FDTD simulation (blue) and coupled-mode theory (red). 92

List of Tables

2.1 Table of gap-midgap percents for fcc, diamond, and tetrastack photonic crystals. 30

4.1 Table of optimized front-coating designs for one, two, and three front-coating layers, as in Fig. 4-1(b). Layers are ordered from closest to air. Coating thickness d in units of nm. 68

Chapter 1

Introduction

Photonic crystals are media that interact with light via a wavelength-scale periodic refractive index modulation [3, 4, 5], illustrated in Fig. 1-1. This opens exciting possibilities in the manipulation of light including negative refraction [6, 7], invisibility cloaks [8, 9, 10], and all-optical computing [11]. The information age we live in today was born from the understanding of the electronic properties of semiconductor crystals. One can imagine similar control over light would open the possibility of new technological breakthroughs just as solid state in the past. In this thesis I will discuss the search for an easily fabricated photonic crystal with a full three-dimensional bandgap, the novel properties of states around certain zero-group velocity modes, and how photonic crystals can be used to modify both the absorptivity and emissivity spectra of material systems. It is of interest to note that while we have recently discovered photonic bandgap materials, nature has been utilizing them for eons, visible in the iridescence of butterfly wings [12, 13] beetle scales [14], and sea worms antenna [15].

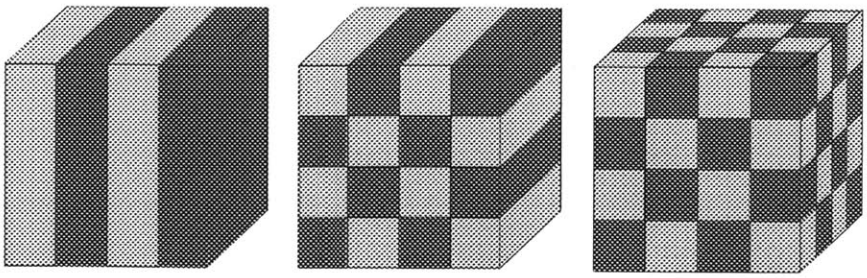

Figure 1-1: From left to right, one-, two-, and three-dimensional photonic crystals. Red and blue denote regions of low and high index.

1.1 The photonic crystal in detail

Since photonic crystals are periodic media, an analogy with semiconductor crystals can help us understand their signature property: the photonic bandgap. In a semiconductor an electron sits in the periodic potential of the positive ions. Quantum mechanics tells us the electron is a wave, and the electron wave experiences multiple coherent scatterings that can constructively interfere in certain directions allowing it to propagate undeflected [16]. For a certain range of electron energy values complete destructive interference occurs and there can be no propagating solutions to Schrodinger's equation; an electronic bandgap is said to open up in this range of energy values. Similarly, in a photonic crystal an electromagnetic wave experiences a multiple coherent scatterings due to the periodic index modulation and can propagate in certain directions undeflected. There may also exist certain frequencies that do not correspond to a propagating solution. This band of frequencies is called the photonic bandgap. In other words, a normally transparent material can be made in a mirror! Moreover, just as doping a semiconductor crystal with atomic impurities whose energy lies within the electronic bandgap of the host can create spatially localized states, engineering a defect in a photonic crystal can create a spatially localized

electromagnetic state [5]. This is only the beginning of the kind of control we can achieve.

Let us dig in a little deeper; by assuming a harmonic time-dependence and rewriting Maxwell's equation as a Hermitian eigenvalue problem we obtain a Hamiltonian for the photon,

$$\nabla \times \frac{1}{\varepsilon(\mathbf{r})} \nabla \times \mathbf{H} = \frac{\omega^2}{c^2} \mathbf{H} \tag{1.1}$$

where $\mathbf{H}$ is the magnetic field, $\varepsilon(\mathbf{r})$ describes the dielectric, ω the angular frequency, and c the speed of light. Due to the periodic boundary conditions, the solutions to Eq. 1.1 appear as bands giving rise to the photonic bandgaps. The states adjacent to a bandgap display qualitative difference; those that are below store most of the electric field energy in the high dielectric region and those above the bandgap store most of there electric field energy in the lower dielectric region. New opportunities open up with the band gaps– sub-wavelength confinement and guiding of light[5, 3, 4, 17], slow light[18, 19, 20], and omni-directional reflection [21, 22]. For crystals with a bandgap, the termination of the crystal can allow solutions that are localized on the surface. (Such surface states are the subject of Chapter 5.)

Since a photonic crystal possesses periodic translational invariance, a crystal wavevector can be associated for each solution,

$$\mathbf{H}_{\mathbf{k}}(\mathbf{r}) = e^{i\mathbf{k}\cdot\mathbf{r}} \mathbf{h}_{\mathbf{k}}(\mathbf{r}), \tag{1.2}$$

where $\mathbf{k}$ is the Bloch wavevector and $\mathbf{h}_{\mathbf{k}}$ is a periodic function. Because there is only periodic translational invariance, the unique set Bloch wavevectors live within a unit cell of k-space, the Brillouin zone. The set of all solutions to Eq. 1.1 can be expressed as a relation between the frequency and wavevector, the band structure.

However, symmetries of the real space lattice can be exploited to drastically reduce the number of points in reciprocal space needed to find bandgaps. Once this reduction of the Brillouin zone is accomplished, the frequencies of the allowed solutions can be plotted versus the crystal wavevector along the high symmetry planes of the irreducible Brillouin zone, Fig. 1-2. Unlike a homogeneous medium with ellipsoidal equifrequency surfaces, photonic crystals possess more complex dispersion relations and equifrequency surfaces. Moreover, the gradient of the equifrequency surface gives the group velocity,

$$\mathbf{v}_g = \nabla_{\mathbf{k}}\omega(\mathbf{k}). \tag{1.3}$$

This opens the way for novel properties such super-collimation [23], all-angle negative refraction [7], and spinning photonic states [24]. A complete understand these novel properties will allow us to use them to enable new behaviors of older technologies.

While there are many similarities with the electronic case, differences arise. One key difference from the electronic case is the photonic Hamiltonian and it's solutions are scale invariant, solutions at one frequency may be scaled up or down simply by scaling the geometry appropriately. This flexibility allows the researcher to place these bandgaps at any frequency they choose provided that all lengths are scaled accordingly and the same epsilon values can be found at those frequencies.

1.2 Thesis overview

Here, I give a brief overview of the contents of the chapters, motivating each chapter and highlighting key results. In Chapter 2 I describe a realizable colloidal photonic crystal, "tetrastack", composed of tetrahedron-shaped particles that possesses a robust, complete bandgap even for small index contrasts [25]. Next in Chapter 3 I

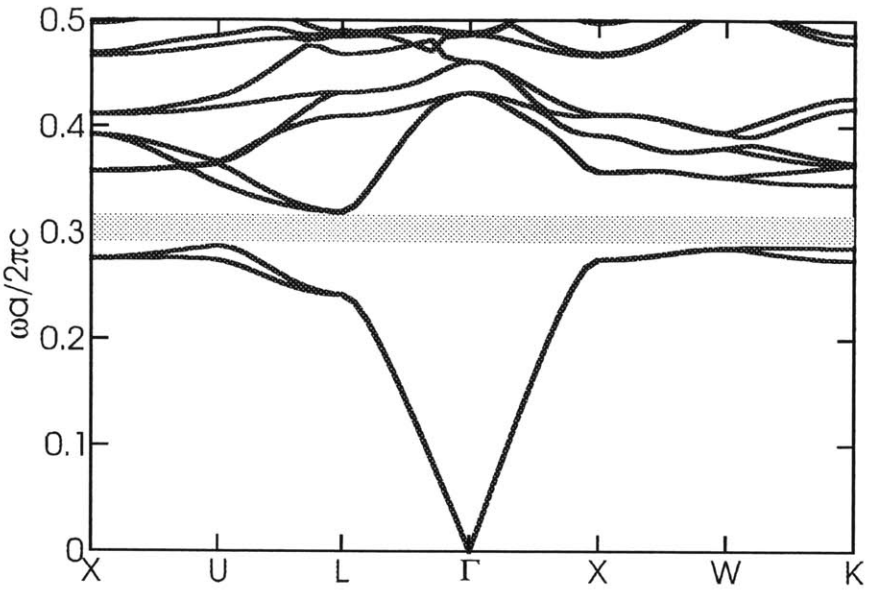

Figure 1-2: Band structure of a three-dimensional photonic crystal. The photonic bandgap is highlighted yellow.

show using a quantity that measures the angle between the group velocity and averaged wavevector that there exists states around certain zero-group velocity points where the angle is obtuse [26]. A physical manifestation of this unusual character is given. In Chapter 4 the optimal benefit of thin front coatings on thin silicon is determined and found to be over 50% even for just two front coatings [27]. Finally in Chapter 5 I show how with a few geometrical parameters, the emissivity spectra of metals can be tailored at will with photonic crystals, opening the way for higher efficiency thermophotovoltaic systems [28].

Though there has been much theoretical and computational advance since 1987, fabrication of photonic crystals is still laborious. Cheap, scalable fabrication of photonic crystals with a full three-dimensional band gap has remained elusive. The techniques that work well for one- and two-dimensional crystals, thin film deposi-

tion techniques such as physical and chemical vapor deposition, and molecular beam epitaxy, and photolithography and etching, require much effort for building three-dimensional crystals. An attractive alternative presents itself in self-assembly.

Self-assembly is an attractive route for building three-dimensional crystals since uniform building blocks can be made in large quantities and can be arranged into a crystalline pattern by allowing the particles to settle with minimal direct guidance. This process is good enough for nature to take advantage of it– opals are self-assembled photonic crystals of silica spheres with lattice constants on the order of 100 nm, giving rise to diffraction in the visible range. However, monodispersed spheres tend to settle into a closed-packed face-centered cubic structure which does not't have a bandgap for any value of index contrast[5]. Moreover a diamond-like structure, which possesses a robust bandgap, is not a thermodynamically favored structure and will not form via self-assembly. In Chapter 2 of this thesis I show that crystals made of non-spherical particles allow a bandgap to open. The most promising of these non-spherical particles is "tetrastack", a particle with four fused spheres in a tetrahedron. Moreover due to the control over the sphere size and amount of fusion one could create the bandgap over a wide range of frequencies. A group theoretic explanation for the properties of a tetrastack crystal is given, and the effect of orientational disorder is explored.

In the third chapter I identify and explore certain anomalous regions in the band structure in two-dimensional photonic crystals. In nature we find that homogeneous media have positive index, and the group velocity and phase velocity (or equivalently the wavevector) of light travelling in these media are parallel to one another. In negative index media, recently realized in certain meta-materials [29], the group velocity and phase velocity point in exactly opposite directions allowing light to do unusual things including negative refraction, superlensing, and anomalous Cerenkov radiation

[30, 31]. Periodic media such as photonic crystals possess band structures that at first sight appear to have modes with opposite group velocity and wavevector. However the wavevector is a crystal wavevector which does not correspond to a phase velocity and can be made to point in any direction by adding a reciprocal lattice vector. For one-dimensional crystals we will see that a mode with negative group velocity and positive wavevector is actually one with negative effective wavevector. In higher dimensional crystals, however, it may be possible to find modes with group velocity and effective wavevector making an obtuse angle with each other. Such modes have never before been identified in positive effective index media. In Chapter 3 I will define a measure of the effective wavevector and show that indeed there are certain regions in the band structure where the angle it makes with the group velocity is obtuse. These novel regions are associated with a particular type of zero-group velocity mode. In addition, we will see that around those special zero-group velocity modes it is possible to make mirrorless cavities of unusually high quality factors.

The last two chapters conclude with shaping the spectral response of materials to boost the efficiency of photovoltaic cells. A thermal source of photons, such as the Sun, illuminates a photovoltaic diode that converts a portion of the incoming energy to electrical power. However without modifying the absorptivity of the PV diode or the emissivity of the source, much of the energy is lost through reflection or deleterious heating. In the case of a silicon solar cell, much effort has gone into decreasing the losses to such an extent that efficiencies for thick silicon solar cells approach the fundamental limit set by detailed balance and silicon's material properties [32, 33]. However, thick, crystalline silicon is expensive and the use of thin (about 1 μm), crystalline or micro-crystalline silicon is becoming increasingly cost-competitive. In Chapter 4, I consider what improvements in efficiency can be made with multiple, thin front and back coatings on a thin silicon cell. Unlike thick silicon cells where

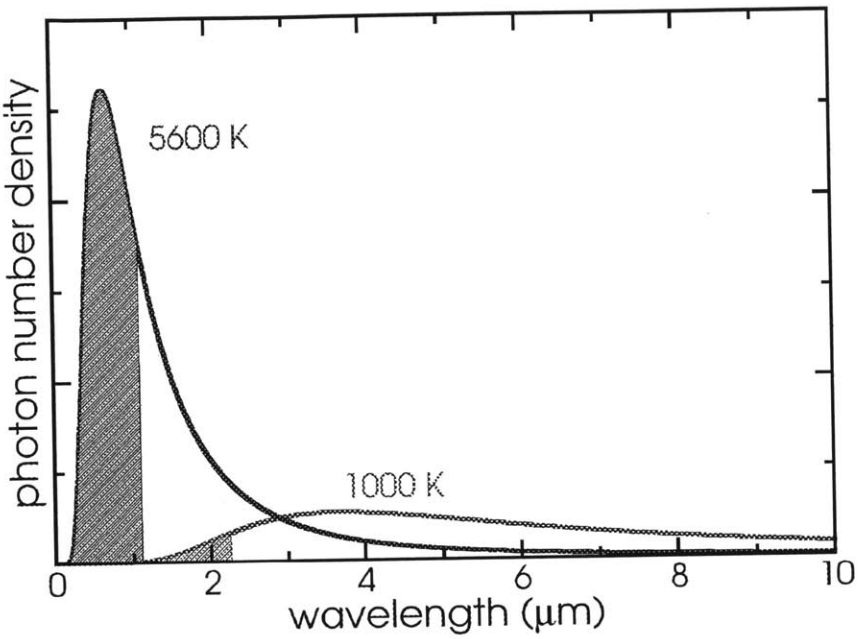

Figure 1-3: Photon number flux per unit wavelength of two blackbody emitters, one at 5600 K (blue) and another at 1000 K (red). The spectrum of the cooler emitter has been rescaled by 100. Shaded regions denote useful photons for a silicon (blue) and InGaAsSb (red) PV diode.

any transmitted light is absorbed, thin silicon cells present the possibility of interference of reflections from the back surface since a single pass is not always enough to absorb a photon. This presents an unexplored challenge. I show that significant improvements, a nearly 50% relative increase in efficiency over an uncoated cell, can be made with simply two front coatings. Moreover, while one could imagine using many more front coatings, we will see that the majority of the improvements come from just the first few layers.

For a thermal source of photons, such as a blackbody, whose spectral distribution is given by the Planck distribution, a significant amount of power is radiated at frequencies in the infrared, below the bandgaps of most semiconductors, illustrated

in Fig. 1-3. For thermophotovoltaic schemes which use a radiator at temperatures much lower than 5600 K, this is disastrous. Consider a typical power generator using a radiator at 1000 K and indium gallium arsenic antimony (InGaAsSb) as the PV diode; the ratio of useful power to total radiated power is less than 19%. However, by modifying the surface of the radiator, it is possible to tailor its emissivity spectrum to closely match the quantum efficiency of the PV diode.

In Chapter 5 of the thesis I examine a particular type of selective emitter, a two-dimensional array of holes etched onto a metal, and how one could tailor its emissivity spectrum. Though the simplest approach would be to use multiple one-dimensional front coatings, a two-dimensional periodic array of holes offers greater benefits. Moreover the use of multiple materials is problematic since all of them must be thermal stable and non-absorptive at high temperatures. Using a one-dimensional periodicity is not enough since not all polarizations and directions are treated the same. For thermophotovoltaic applications, one would like a thermal emitter with minimal emissivity in the infrared and a high melting point. Refractory metals, including tungsten, satisfy both requirements. The hole array creates photonic resonances, solutions to Eq. 1.1 with a complex frequency, that are localized to the surface. The key to the selective emissivity is that the resonances exist only above a cutoff frequency that is determined by the geometrical parameters. In addition, the geometrical parameters determine how strongly these resonances radiate. I look at how one can analytically predict where these photonic crystal resonances exist and their lifetimes, which allow one to compute the emissivity spectrum via a scattering matrix framework, i.e., temporal coupled-mode theory. To study this problem more efficiently the absorption spectrum is calculated– Kirchhoff's law states that the absorptivity and emissivity are the same for an object in thermal equilibrium. While computational methods for computing the absorptivity spectrum, such as

finite-difference time domain or finite-element methods, yield accurate results, they are computationally intensive. Once one can semi-analytically compute the absorptivity spectrum, then optimization of the spectrum for thermophotovoltaic systems and other applications becomes possible.

Chapter 2

Tetrastack: colloidal photonic crystal

Photonic crystals strongly localize photons of certain frequency, offering a novel means to control light [5]. This control over light is achieved via the periodic refractive index modulation of the photonic crystal which allows a photonic bandgap to open in a manner analogous to the electronic bandgap of a semiconductor crystal. While photonic crystals are expected to enable the production of high performance optoelectronic devices– lossless waveguides [34], photocatalysts based on extended lifetimes of excited species [35], low threshold, highly efficient semiconductor lasers [36], and nonlinear optical switches [37]– few structures have been found that possess the *complete* 3D photonic band gap required for the promised degree of light control. Here one possible solution based on a colloidal photonic crystal is described. The building block are colloidal tetrahedra arranged in a fcc lattice. A robust omnidirectional bandgap is found and compared to diamond.

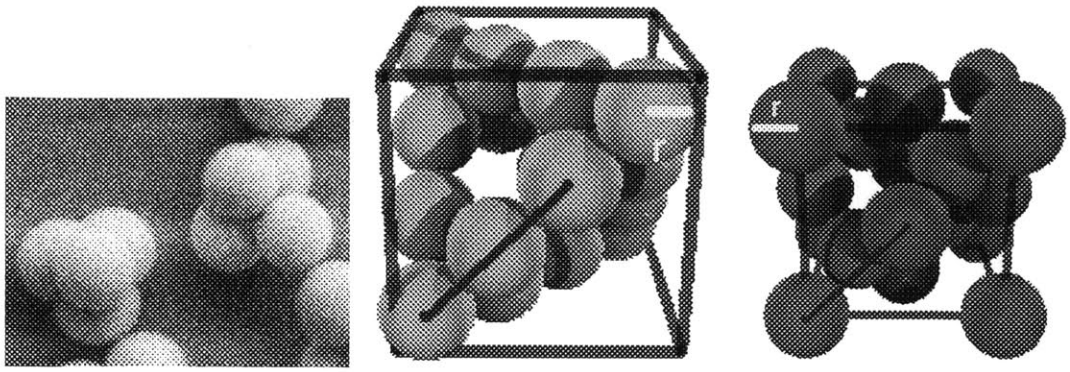

(a) (b) (c)

Figure 2-1: (a) SEM images of fabricated tetrahedral colloidal particles. (b) Tetrastack particles at the lattice points of the photonic crystal. (c) Conventional unit cell of diamond photonic crystal.

2.1 Introduction

Three-dimensional (3D) periodic structures have been successful made at the micron length scales corresponding to bandgaps in the infrared [38], however it remains a challenge to easily fabricate photonic crystals at the submicron length scale necessary for devices operating within the visible and near-infrared region. Producing such photonic crystals requires the fabrication of lattice elements with a feature size of a few hundred nanometers. Relative to 3D lithography approaches [39, 38], colloid-based solutions for the fabrication challenge are highly attractive due to the ease of accessing the submicron size regime and relative low cost for the buildup of 3D structures. Colloidal photonic crystals have been fabricated with a periodicity of about 170nm which display a partial photonic band gap in the violet-ultraviolet, a feat not yet duplicated with lithographic based photonic crystals [40].

Self-assembly of monodispersed spheres leads to energetically favorable structures with high packing density which includes face-centered cubic (fcc). The fcc structure,

however, has no bandgap irregardless of the refractive index contrast n_c between the spheres and the surrounding medium due to degeneracy at the W k-point. On the other hand, the inverted fcc structure, a lattice of air spheres in a high index medium, i.e., inverse opal, can possess a bandgap between the 8th and 9th bands for a refractive index constrast of at least 2.9 [41, 42]. The utility of higher order bandgaps is lessened since such bandgaps are sensitive to all types of geometric disorder including variations in the radii of the spheres and random displacements from lattice sites. Small amounts of disorder in the lattice constant amounting to a few percent can completely destroy the bandgap. Lower lying photonic band gaps, such as the one in diamond, are much more robust to disorder.

2.2 Tetrastack

Wide and robust photonic bandgaps between the second and third bands open for the diamond and inverted diamond crystal structures with relatively low index contrasts [43]. However neither are thermodynamically favorable colloidal structures and do not form naturally. Recently, a pick-and-place nanorobotic method of building a colloidal diamond structure was demonstrated; however the crystal was composed of just 165 silica spheres each taking an average of 3.8 minutes to place [44]. Alternatively, non-close-packed structures with diamond-like connectivity could be realized using colloidal cluster building blocks, with the "openness" of the final crystal structure and the mechanical stability provided by the geometry of their packing. Nonspherical colloids also offer reduced symmetry at the lattice point, a feature thought to promote the large stable band gap in the diamond structure [43]. Knowledge of the photonic properties of crystal structures based on colloidal cluster building blocks is limited, since only the diamond-like dimer structure has been explored in modeling

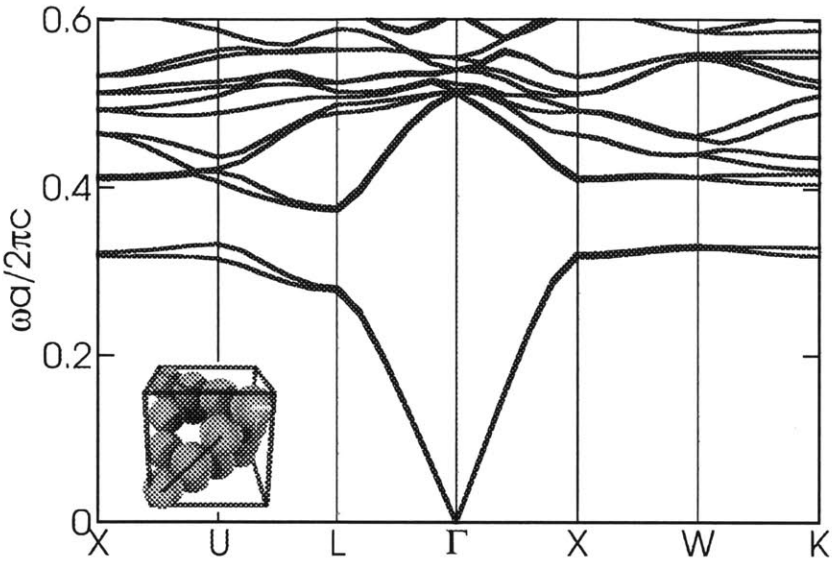

Figure 2-2: Band structure of inverted tetrastack in silicon ($n_c = 3.4$) with sphere radius $0.27a$. Inset, a portion of the tetrastack photonic crystal unit cell.

studies of the photonic bands [44, 45]. The present theoretical study reports robust photonic bandgaps for a diamond-inspired crystal structure with a nonspherical, colloidal tetrahedron basis. The plane wave expansion method with more than 4000 plane waves (corresponding to a resolution of 16 pixels per a) was used to calculate photonic band structures for the newly proposed "tetrastack" by solving Maxwell's equations in the frequency domain [46]. The minimum refractive index contrast to open at least a 1% complete 3D-photonic band gap in the inverted tetrastack structure was found to be 1.94, making this one of the lowest threshold refractive index-contrast photonic crystal structures discovered. A more relaxed requirement for the refractive index contrast enlarges the range of materials appropriate for fabricating structures with omnidirectional photonic band gaps [47].

The tetrastack photonic crystal structure is composed of tetrahedral colloidal clusters stacked to connect nearest neighbor sites in the fcc lattice where each sphere of a tetrahedron connects to a neighboring site. Figure 2-1(a) and Fig. 2-1(b) depicts the tetrastack structure in comparison with the diamond structure Fig. 2-1(c). The real-space structure is described as an fcc lattice with lattice vectors $\mathbf{R}_1 = a/2\,(\hat{\mathbf{y}}+\hat{\mathbf{z}})$, $\mathbf{R}_2 = a/2\,(\hat{\mathbf{x}}+\hat{\mathbf{z}})$, $\mathbf{R}_3 = a/2\,(\hat{\mathbf{x}}+\hat{\mathbf{y}})$, where a is the length of the conventional cubic cell. The tetrahedron spheres are at positions, $\mathbf{0}$, $\mathbf{R}_1/2$, $\mathbf{R}_2/2$, and $\mathbf{R}_3/2$. One threefold symmetry axis of each tetrahedron points along the main diagonal of the fcc lattice, reducing the symmetry group of each lattice point from O_h (full octahedral group) to T_d (tetrahedral group). Figure 2-2 shows the band structure calculated for the inverted tetrastack structure of air tetrahedra in a silicon matrix. As in the case of the diamond structure, the degeneracy between the second and third photonic bands at the W point for the fcc lattice is replace with a degeneracy in the first and second bands and a degeneracy in the third and fourth bands [45]. Therefore a sizable bandgap can open for the appropriate combinations of refractive index contrast and solid volume filling fraction f.

Table 2.1 compares the relative bandgap width $\Delta\omega/\omega_{\text{center}}$ of tetrastack structures with those of the diamond and fcc structures and their inverted counterparts. Refractive index contrast values for zinc sulfide-air ($n_c = 2.29$) and silicon-air ($n_c = 3.41$) were used in the calculations for both direct and inverted structures. Solid volume filling fractions that maximized the band gap for each structure were selected. Comparable bandgap widths were found for inverted tetrastack and inverted diamond structures, 25.3% and 26.9%, respectively. The bandgaps were much larger than those for the corresponding inverted fcc structures at the same index contrast.

A wide range of solid volume filling fractions were found to exhibit full photonic bandgaps for tetrastack structures, as shown by the band gap maps in Fig. 2-3 for

Structure	n_{hi}	fill-fraction	Gap-Midgap %
Tetrastack	2.29	0.46	3.2
	3.41	0.43	13.7
Inverted Tetrastack	2.29	0.28	8.4
	3.41	0.21	25.3
Diamond	2.29	0.43	3.7
	3.41	0.41	12.9
Inverted Diamond	2.29	0.28	8.9
	3.41	0.20	26.9
Inverted FCC	2.29	0.28	0
	3.41	0.28	4.8

Table 2.1: Table of gap-midgap percents for fcc, diamond, and tetrastack photonic crystals.

ZnS-air and Si-air materials. Constituent spheres touch at a solid volume filling fraction of 0.37 for direct tetrastack and 0.34 for direct diamond. Five distinct regions corresponding to structures of the same refractive index contrast, symmetry group, and connectivity of solid material can be identified in Fig. 2-3. The variety of structures represented by the area of the gap map is nearly as broad for tetrastack structures as for diamond structures. In particular, inverted structures of the same index contrast display wider bandgaps than their direct counterparts.

The effect of refractive index contrast on relative bandgap size near the solid volume filling fractions that optimize the bandgap for each structure is presented in Fig. 2-4. The bandgaps naturally fall into three groups corresponding to the connectivity of the high index region. The threshold refractive index contrast needed to create a full photonic bandgap is $n_c = 2.1$ for direct tetrastack with $f = 0.42$ and $n_c = 1.94$ for an inverted tetrastack with $f = 0.30$. This is one of the few predictions of a full photonic bandgap in the case of a structure with a refractive index contrast lower than 2. Large bandgaps of 10% or more can be obtained at index contrasts

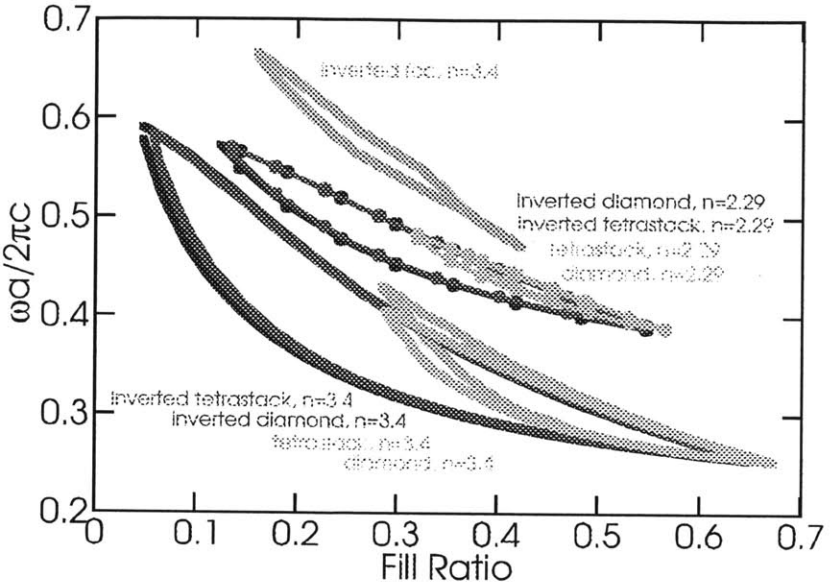

Figure 2-3: Bandgap map of ZnS-air ($n_c = 2.29$) and Si-air ($n_c = 3.4$) colloidal structures.

that are insufficient to open a bandgap in the inverted fcc structure of air spheres.

For the structure composed of a colloidal dimer basis made from silicon, Li, Wang, and Gu [48] determined a relative bandgap width of 15.5% relative to the center frequency when the major axis of the dimer was oriented along the (111) direction and the solid volume filling fraction was 0.34. Note that for these parameters the dimer structure is equivalent to diamond. The bandgap was reduced to half its maximum value for a deviation angle of 5° from the main diagonal. In a similar manner the dependence of the photonic band structure on the tetrahedra orientation in the tetrastack structure was studied by calculating the relative bandgap width as the symmetry axis of the tetrahedra rotates from the (111) direction toward the (100) and (110) directions. Similar to the case of the diamond-analog dimer structure, the bandgap is maximized when the axes of the tetrahedra are oriented along the (111)

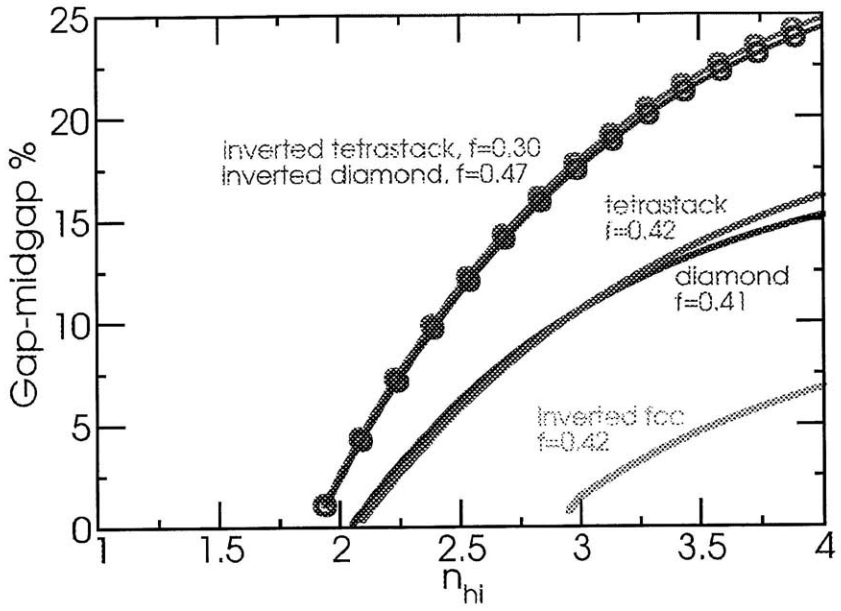

Figure 2-4: Relative bandgap size versus index constrast for various structures at filling fractions corresponding to optimal relative bandgaps.

direction, Fig. 2-5. The bandgap persists for the inverted tetrastack up to an angle about halfway between the main diagonal and a face diagonal. The bandgap width decreases to half of its original value for the ZnS-air system at a deviation angle of 11° – 12° for inverted tetrastack and 5° – 6° for direct tetrastack. Thus a less severe design requirement is predicted for orientation of the tetrahedra in inverted tetrastack than for dimers in the diamond-analog structure.

2.3 Fabrication of tetrastack

Up to 10^{10} colloidal cluster building blocks have been prepared using an emulsion trapping method [49] or a microfluidic confinement cell where specific configurations were determined uniquely by the particle diameter relative to the dimensions of

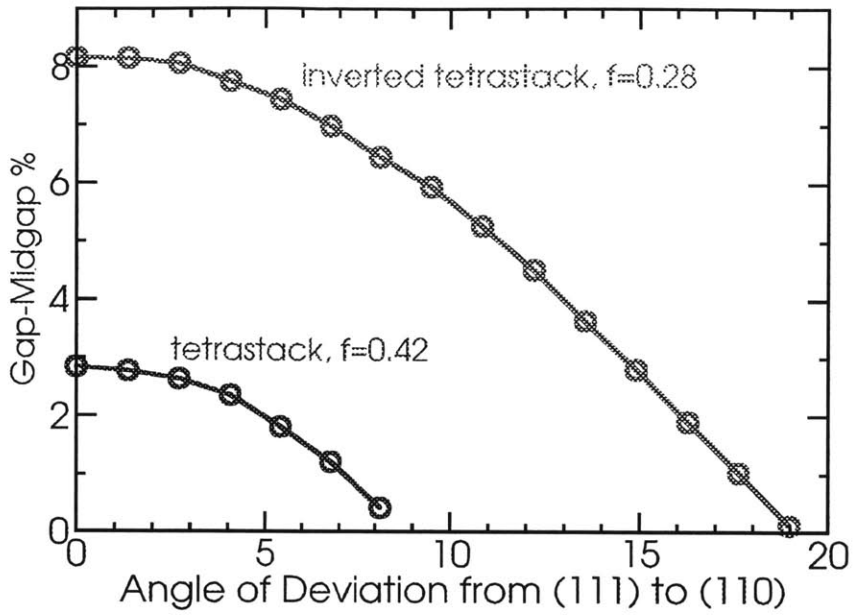

Figure 2-5: Rotating the tetrastack particles away from the unit cell main diagonal (111) to a face diagonal (110) reduces the size of the bandgap.

lithographically defined holes [45, 50]. Similarly, Hammond and Lee [51] utilized a patterned template of positively charged polyelectrolyte dots to capture beads from a suspension of negatively charged carboxylated polystyrene and to create specific configurations of clusters determined by the bead diameter and the pattern dimensions. The clusters would be useful for nonspherical bases in inverted structures, but would not be appropriate for direct structures with a complete bandgap due to the low refractive index of the polystyrene building block, $n = 1.6$ [52].

An alternative method is to use tetrahedral clusters made through the controlled coalescence of high-index building blocks during their chemical synthesis as demonstrated for ZnS by Liddell [53]. Zinc sulfide spheres ranging from 0.5 to 2μm in diameter were clustered into dimers, trimers, and tetrahedra Fig. 2-1(a) using the

decomposition of thioacetamide at elevated temperatures in the presence of the metal salt. The ZnS particles exhibited a refractive index of $2.09-2.25$ in the visible region [54]. While optical tweezers could be used to prepare ordered structures from the building blocks [48], directed assembly in electric, magnetic, and hydrodynamic fields [55] may be less laborious. A possible route toward fabricating a tetrastack colloidal crystal would be via a layer-by-layer convective assembly of tetrastack particles onto a compliment polyelectrolyte dot pattern [51]. A sacrificial film is then deposited onto the first layer of tetrastack particles to prevent the next layer from settling into the interstitial spaces between the first layer of tetrastack particles. Finally the polyelectrolyte pattern could be restamped to repeat the process until the target number of layers is achieved.

In conclusion, a new experimentally attainable colloidal photonic crystal with a full and robust photonic bandgap has been described. Moreover for a range of refractive index contrasts, filling fraction, and tetrahedron orientation a bandgap will remain. Thus photonic crystals made from colloidal structures have the ability to substantially widen the range of realizable full 3D bandgaps.

Chapter 3

Distinguishing zero-group velocity modes in photonic crystals

3.1 Introduction

Propagation of light in photonic crystals can be quite different from that in homogeneous media, such differences include photonic band gaps, supercollimation, superprism effects [23], and extraordinary or negative refraction [7]. Most of these effects are closely associated with an unusual feature of the dispersion relation (band structure), the frequency ω versus wavevector $\mathbf{k}$, of periodic systems: there are extrema, or points of zero group velocity $\nabla_{\mathbf{k}}\omega$. Such points do not occur in a homogeneous medium, only in localized modes of certain waveguide structures or in non-localized modes of periodic media. Since extrema in the frequency bands are so central to the unique phenomena possible in photonic crystals, we wish to investigate them more closely, and to ask the question: are there significant *qualitative* differences between different band extrema, and what relationship do these differences have to various

physical phenomena? Naturally, there are some obvious qualitative differences: some extrema are maxima, some are minima, and others are saddle points. And, of course, the exact eigenmode solutions in the vicinity of the extrema provide, in principle, complete information about their behavior. But the latter is too much information—we would hope to have a simpler description of the differences between extrema than the entire field patterns—and the former is too little, as we shall see. In particular, we will argue that there are substantial differences between extrema at high-symmetry $\mathbf{k}$ points (such as the center or edge of the Brillouin zone, corresponding to the traditional criteria for Bragg diffraction) and extrema at other $\mathbf{k}$. And, even among these non-symmetric extrema, there are distinct differences between those arising from avoided eigenvalue crossings (anti-crossings) and other band-repulsion phenomena. As we will show these differences arise from general properties of periodic crystals, therefore such differences in zero–group-velocity should be found in other periodic systems, including electronic and phononic crystals.

In order to have a quantitative measure of these differences independent of any particular physical phenomena, we consider by analogy an important quantity of homogeneous media that is ill-defined in periodic structures: the phase velocity $\mathbf{v}_p = \omega\mathbf{k}/|\mathbf{k}|^2$. In a homogeneous medium, the relative direction of the phase and group velocities reveals important information such as whether the medium is right- or left-handed (negative index) [30] and to what degree the medium is isotropic. In a periodic medium, the phase velocity is ill-defined because $\mathbf{k}$ is not unique—it is equivalent to $\mathbf{k}+\mathbf{G}$ for any reciprocal lattice vector $\mathbf{G}$ [5]. Equivalently, an eigenmode in a periodic structure corresponds to an infinite number of Fourier components $\mathbf{k}+\mathbf{G}$, given by the Fourier-series expansion of the Bloch envelope, each with its own "phase velocity". However, we can use the *amplitudes* of these Fourier components, $\mathbf{H}_{\mathbf{k}+\mathbf{G}}$, to quantify the *degree* to which the solution resembles that of a homogeneous medium

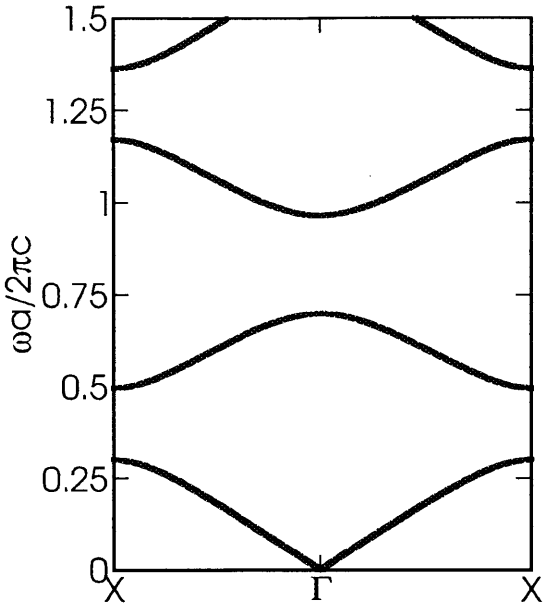

Figure 3-1: Typical 1D band structure for a Bragg mirror with high dielectric $\varepsilon = 9$ and width $d = 0.2a$

and the degree to which the "average" phase velocity is parallel to the group velocity, and we find that this average exhibits interesting distinctions between different band extrema. In particular, we define

$$\eta_{\mathbf{H}} = \frac{\sum_{\mathbf{G}} \frac{\mathbf{v_g}}{|\mathbf{v_g}|} \cdot \frac{(\mathbf{k+G})}{|\mathbf{k+G}|} \mid \mathbf{H_{k+G}} \mid^2}{\sum_{\mathbf{G}} \mid \mathbf{H_{k+G}} \mid^2}. \tag{3.1}$$

as a measure of the anomalous character of a mode. $\eta_{\mathbf{H}}$ is bounded between -1 and 1, since it is a sum of cosines of the angle between the group velocity and the wavevector weighted by the Fourier component amplitude. A positive (negative) sign indicates normal (anomalous) character; in fact in the homogeneous, right-handed medium limit $\eta_{\mathbf{H}}$ is 1 for all modes. The form of this function is somewhat arbitrary, e.g. one could just as easily use the electric field instead of the magnetic field, but as we'll

see later, alternative definitions of η yield similar qualitative results.

This difference has a physical consequence; as we'll see shortly the difference zero-group velocity modes give rise to very different light confinement behavior. This behavior is connected to the information presented in $\eta_{\mathbf{H}}$.

3.2 $\eta_{\mathbf{H}}$ in 1D photonic crystals

Consider first a one-dimensional photonic crystal, such as a multilayer film of period a with alternating $\varepsilon = 9$ (thickness $0.2a$) and $\varepsilon = 1$ (thickness $0.8a$), whose band structure $\omega(k)$ (solved using a planewave method [46]) is shown in Fig. 3-1. In such a structure, there are bands that have opposite-signed group velocity and k and which therefore appear "anomalous," but examining $\eta_{\mathbf{H}}$, plotted in Fig. 3-2(a), reveals that they are not. The first band is clearly positive throughout the Brillouin zone. Moreover, it is the only band in which $\eta_{\mathbf{H}}$ approaches a constant non-zero value as k vanishes, behavior due to the fact that v_{g} approaches a constant non-zero value at low frequencies. The second band, which looks anomalous since v_{g} is opposite to k in the first Brillouin zone, is shown to be "normal" in the sense of $\eta_{\mathbf{H}}$: most of its Fourier components actually lie at negative wavevectors, aligned with v_{g}. Since all other bands have the behavior of one of these two bands, it appears that all one-dimensional modes have similar, normal character.

Fourier decomposing the modes of the second band shows the lack of any anomalous character more explicitly. In Fig 3-2(b) the various Fourier components of the second band are plotted. The Fourier component $Ga/2\pi = -1$ is over 60% for most of the Bloch modes between $ka/2\pi = 0$ and 0.5. Effectively the mode at k behaves like a plane wave with $k = k - 2\pi/a$. So the group velocity and "average" k point in the same direction. For vanishing k, the modes begin to have an additional mirror

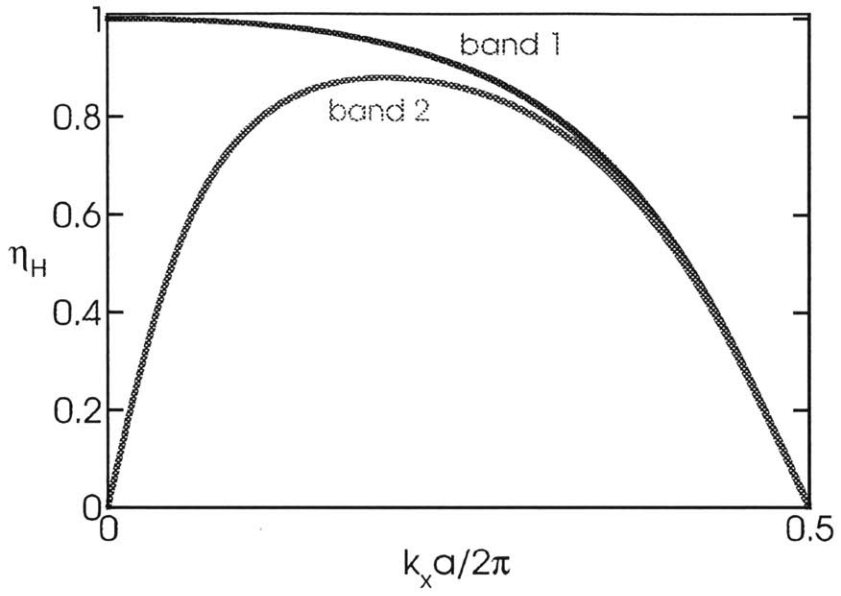

(a)

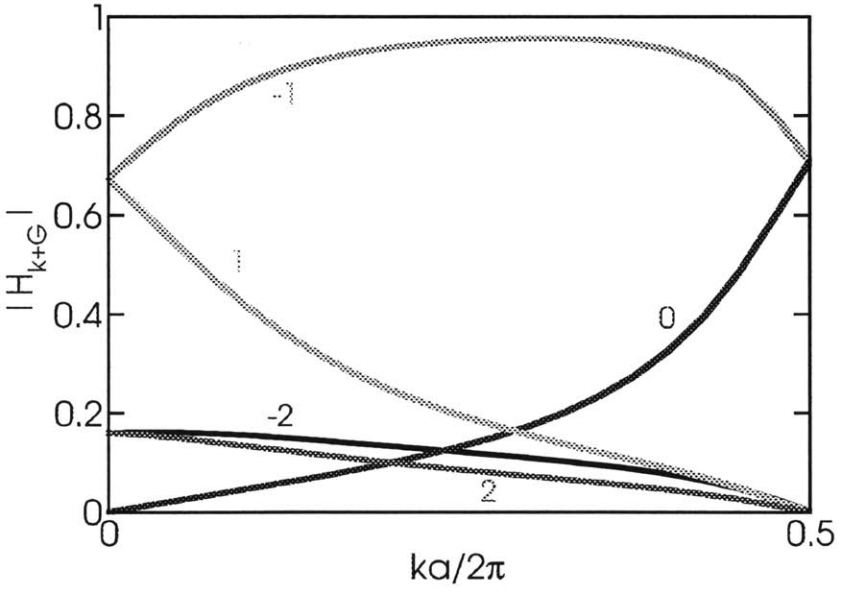

(b)

Figure 3-2: (a) $\eta_{\mathbf{H}}$ calculated across the 1st and 2nd bands. (b) The magnitudes of the dominant Fourier components across the second band of Fig. 3-1. Away from the band edges, where strong mixing occurs, the second band behaves as a plane wave with $ka/2\pi \rightarrow ka/2\pi - 1$.

symmetry plane, so for every G there is a $-G$ component that cancels its contribution to $\eta_{\mathbf{H}}$ ensuring that $\eta_{\mathbf{H}}$ goes to zero.

There is a simple argument why one-dimensional photonic crystals should not exhibit sign changes of $\eta_{\mathbf{H}}$, and therefore should not exhibit negative $\eta_{\mathbf{H}}$ for right-handed materials. To begin with, for a given frequency ω, the allowed wavevectors k in a one-dimensional crystal come from the eigenvalues $\exp(ika)$ of a 2×2 transfer matrix [56], and thus there can be at most two distinct real-k solutions at each ω. This precludes the possibility of having more than two extrema in a given band, and by symmetry (either mirror symmetry or time-reversal symmetry) these two extrema must occur at the Brillouin-zone edges. By the same symmetry, however, $\eta_{\mathbf{H}}$ cannot change sign at these points. The only remaining possibility would be for $\eta_{\mathbf{H}}$ to change sign at a point that is not an extremum, where v_g does not change sign, but this seems unlikely and we have been unable to find such a circumstance.

3.3 $\eta_{\mathbf{H}}$ in 2D photonic crystals

For two-dimensional periodic structures there can be zero–group-velocity modes away from the Brillouin-zone edge or center. For example, a square lattice (period a) of dielectric rods ($\varepsilon = 9$ and radius $r = 0.2a$) in air illustrates this new type of zero–group-velocity mode at $\mathbf{k} = \Sigma$ where Σ lies on ΓM, (Fig. 3-3), which itself can be divided into further subcategories. Around the M-point, repulsion occurs between the second and fourth bands that causes the second band to develop a local minimum, where we might hope to find unusual behavior compared to a homogeneous right-handed medium. The repulsion that drives the second band downward originates in the shared symmetry character of the second and fourth bands under reflection about the mirror plane that contains $\mathbf{k}$ along ΓM. Perturbative analysis of the modes

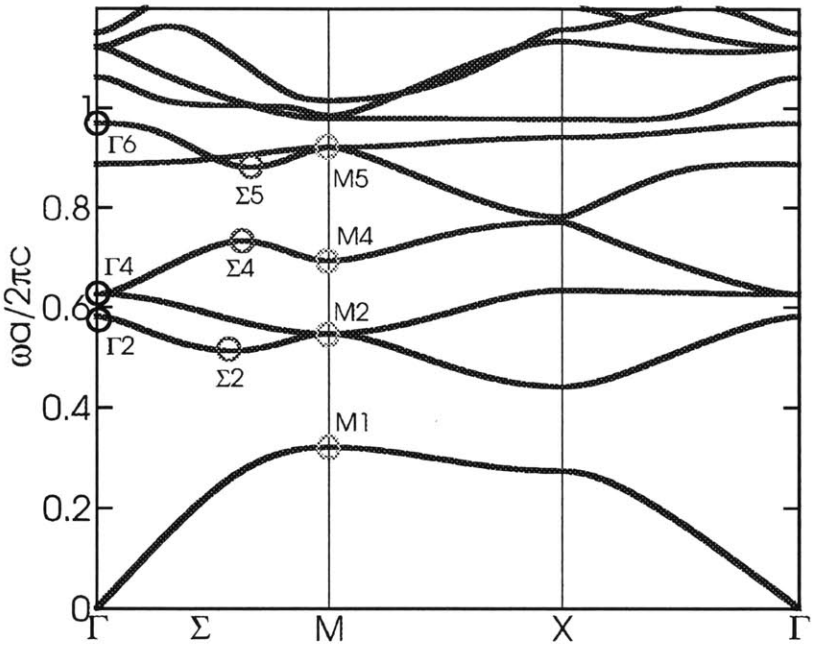

Figure 3-3: 2D band structure with dielectric profile (inset) $\varepsilon = 9$, $r = 0.2a$. Circled are the different types of zero-group velocity points; labels indicate location in the irreducible Brillouin zone and band number.

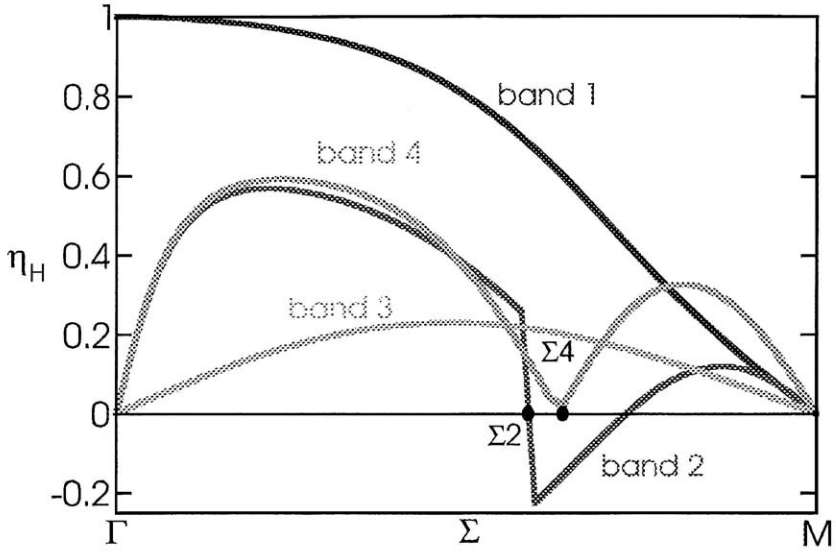

Figure 3-4: $\eta_{\mathbf{H}}$ for the first four bands of the two-dimensional crystal in Fig. 3-3.

near M of the second band, by expanding them in the basis of the eigenmodes *at* M, shows that the second band is indeed composed partly of the fourth mode at M [57]. Another type of zero–group-velocity mode is due to the avoided crossing along ΓM in bands four and five. The difference between these two types of extrema, both located away from the Brillouin-zone edge or center, is evident in $\eta_{\mathbf{H}}$, shown in Fig. 3-4. A small region in the second band has negative $\eta_{\mathbf{H}}$ (which grows if we increase ε to increase the repulsion between the second and fourth bands). In contrast, the anti-crossing in the fourth band does not produce a negative $\eta_{\mathbf{H}}$, though it is responsible for the dip in $\eta_{\mathbf{H}}$. The third band shows that "negative" group velocity (opposite to k in the first Brillouin zone) does not imply negative $\eta_{\mathbf{H}}$.

A look at the amplitudes of the Fourier components, Fig. 3-5(a), explains the

behavior of the second band. Along the second band, one pair of modes dominate for most of the band, and even when the "positive phase velocity" $\mathbf{G}a/2\pi = (0,0)$ component increases in value the "negative phase velocity" $\mathbf{G}a/2\pi = (-1,-1)$ component initially compensates for it. This allows the "average phase velocity" to remain negative and hence allows $\eta_{\mathbf{H}}$ to become negative just after the minimum. For comparison, the third band where the group velocity is always "negative" in this range of k has a Fourier decomposition that is always dominated by one pair of "negative phase velocity" components.

It should be emphasized that the sign of $\eta_{\mathbf{H}}$ does not determine whether there is negative or positive refraction at a (11) interface of the structure. The direction of refraction is not determined by the dominant Fourier decomposition, but essentially by whether the mode has *any* $\mathbf{G} = 0$ Fourier component that an incident wave from a homogeneous medium can couple to at the given Bloch wavevector. Thus, "left-handedness" is not strictly required for negative refraction. For example, in this structure, first two bands are negative refracting near M with a positive $\eta_{\mathbf{H}}$, similar to the structure considered in Ref. [58]. As another example, the negative-refracting modes looked at by Ref. [7], the entire first band is dominated by the $\mathbf{G} = 0$ component, yielding a positive $\eta_{\mathbf{H}}$. (Of course, one can *define* an "effective index" by arbitrarily choosing a phase velocity from $\mathbf{k}$ in the first Brillouin zone [58, 7], but this need not coincide with the average phase velocity determined by the Fourier decomposition.) In uniform cross-section waveguides (in which phase velocity is well defined), modes with group velocity opposite to phase velocity (and hence $\eta < 0$) have also been identified [59]. However, at any given frequency in these waveguides there are always both negative- and positive-η modes, whereas in the crystal considered here it is possible to get only $\eta < 0$ modes in a certain frequency range by tuning the rod radius.

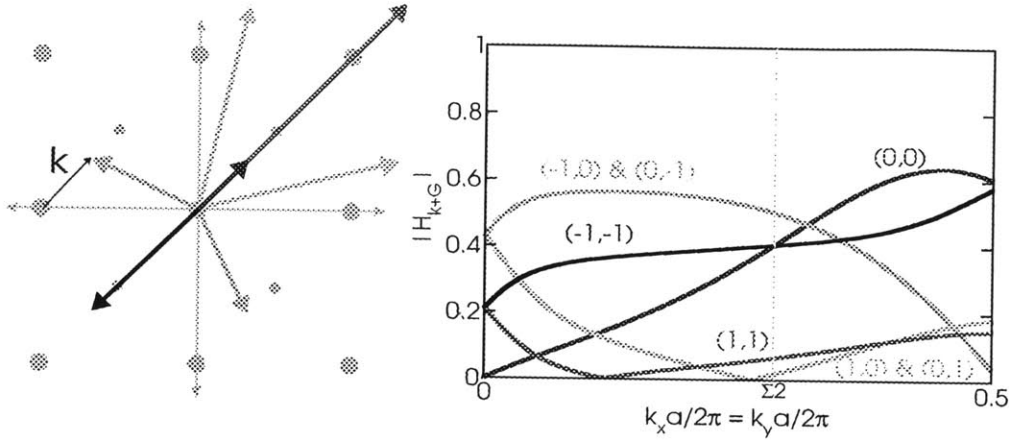

(a)

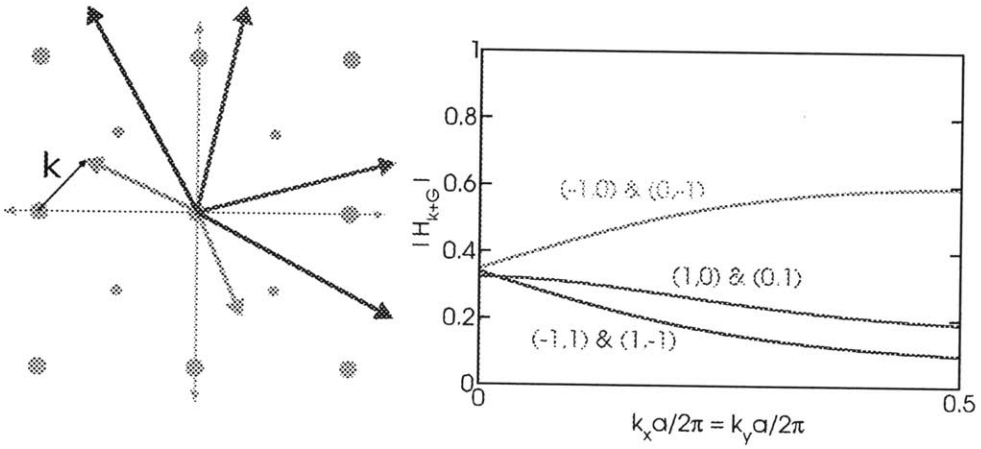

(b)

Figure 3-5: (a) $\mathbf{k} + \mathbf{G}$ associated with the largest Fourier components for the second band, and magnitudes of associated Fourier components across the same band. (b) $\mathbf{k} + \mathbf{G}$ for third band, and magnitudes of associated Fourier components across the band.

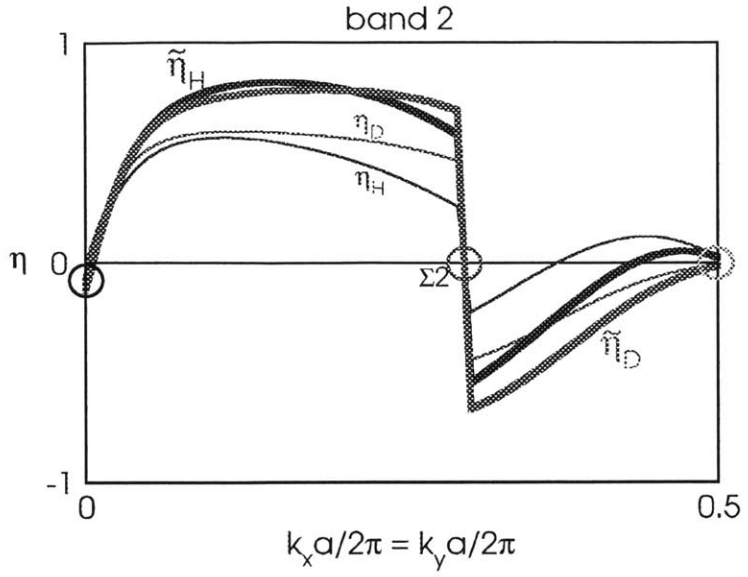

(a)

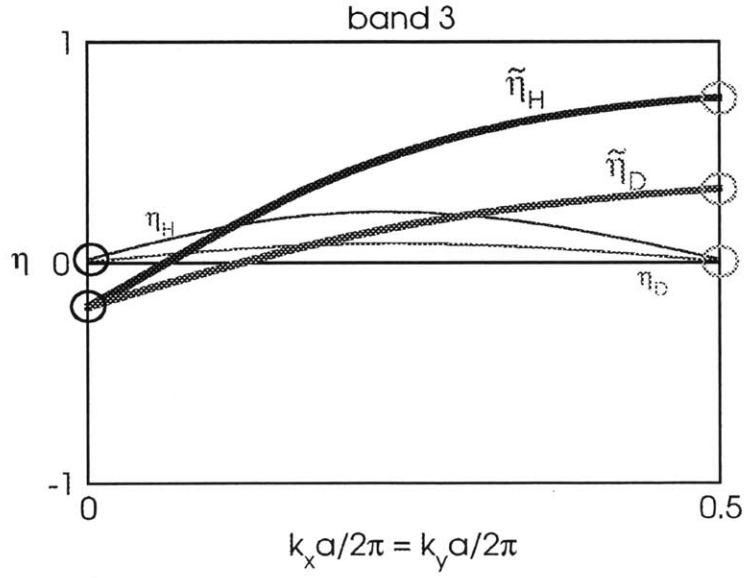

(b)

Figure 3-6: (a) Plot of η (thin lines) and $\widetilde{\eta}$ (thick lines) for the second band. Color indicates the field used as the weight: **H** (blue) and **D** (red). (b) Same comparison but for the third band where behavior is expected to be normal.

To ensure that the behavior exhibited by $\eta_{\mathbf{H}}$ is not an artifact of some arbitrary choice in our definition, we explored other definitions and verified that the qualitative results do not change. For example, one can define $\eta_{\mathbf{D}}$ by simply replacing $\mathbf{H}$ with $\mathbf{D}$, the electric displacement field, in Eq. (3.1). One can also define $\widetilde{\eta}_{\mathbf{H}}$, the difference between the Fourier components with $\mathbf{k}+\mathbf{G}$ making acute angles with $\mathbf{v}_g$ and those with obtuse angles.

$$\widetilde{\eta}_{\mathbf{H}} = \sum_{\mathbf{G}}^{(\mathbf{k}+\mathbf{G})\cdot\mathbf{v}_g \geq 0} |\, \mathbf{H}_{\mathbf{k}+\mathbf{G}} \,|^2 \; - \sum_{\mathbf{G}}^{(\mathbf{k}+\mathbf{G})\cdot\mathbf{v}_g < 0} |\, \mathbf{H}_{\mathbf{k}+\mathbf{G}} \,|^2 \,. \tag{3.2}$$

A corresponding quantity $\widetilde{\eta}_{\mathbf{D}}$ using the Fourier components of $\mathbf{D}$ can also be defined. Figs. 3-6(a)–3-6(b) plot these alternative definitions, compared with $\eta_{\mathbf{H}}$, for bands two and three, and show that the qualitative behavior around the zero–group-velocity point is preserved. The $\widetilde{\eta}$ definitions do become negative near Γ, but this is an artifact of weighting the Fourier components that are only slightly on the "positive" side, such as $\mathbf{G}a/2\pi = (1,-1)$ and $(-1,1)$, equally with very positive Fourier components such as $\mathbf{G}a/2\pi = (1,0)$ or $(1,1)$, rather than weighting them with the dot product $\mathbf{v}_g \cdot (\mathbf{k}+\mathbf{G})$. (Similarly for the fact that the third band has non-zero $\widetilde{\eta}$ at the M point.)

3.4 Mirrorless cavity

One manifestation of the differences between the zero–group-velocity modes can be found in the dependence of cavity quality factors on the cavity length. Here, we are considering the simplest one-dimensional realization of an optical cavity: a slab of some material (or crystal structure) terminated by two mirrors on either end, which

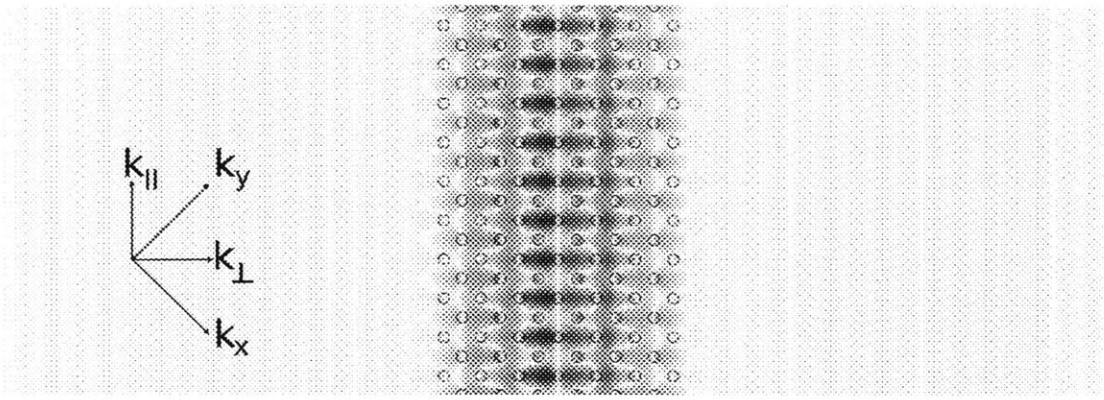

Figure 3-7: Photonic-crystal Fabry-Perot cavity, formed by a finite number of layers of the crystal in the (11) direction. Here, the thickness is $L = 12d$, where $d = a/\sqrt{2}$ is the distance from one row of rods to the next. Blue/white/red indicate positive/zero/negative E_z field of a resonant mode with $Q \sim 2000$.

confines standing wave modes that leak out slowly due the imperfect reflectivity of the ends. Even simpler, we can omit the mirrors and just rely on the innate reflectivity of the interface between the cavity material/structure and the surrounding material (e.g. air). The quality factor Q is a conventional dimensionless lifetime (the number of optical periods for the energy to decay by $e^{-2\pi}$). Normally, the quality factor increases monotonically as the size of a cavity is increased, all other things equal, simply because a smaller portion of the mode is exposed to the edge of the cavity where it can escape (or equivalently because the round-trip time through the cavity increases). However, if the cavity material has a band extremum, more unusual length dependence can occur at frequencies near this extremum. Given the wavevector $\mathbf{k}$ of the extremum, the component of $\mathbf{k}$ perpendicular to the cavity interface $k_\perp$ introduces a length scale $\pi/k_\perp$, and as the cavity length changes by multiples of this length scale there are interference effects that lead to periodic peaks in Q [60]. If the extremum occurs in a periodic medium, however, there are multiple length scales corresponding to the different Fourier components $\mathbf{k} + \mathbf{G}$ (unless one

component dominates), and the phenomena are more complicated. Moreover, in a periodic medium the thickness of the cavity cannot be increased continuously without changing the crystal termination, and so at best one expects periodic peaks in Q at the least common multiple of $\pi/k_\perp$ and the crystal period.

In particular, we consider structures like the one depicted in Fig. 3-7: a finite number of layers of our square-lattice 2D crystal, oriented in the diagonal (11) direction, with thickness L in units of $d = a/\sqrt{2}$ (the distance from one layer to the next along the diagonal direction). This structure is periodic along the vertical $(1\bar{1})$ direction, and so the modes would be characterized by a $k_\parallel$ Bloch wavevector along this direction (parallel to the cavity interfaces), but we only consider $k_\parallel = 0$ modes which couple to normal-incident radiation. Note that for $\omega a/2\pi c < 1/\sqrt{2}$, there are no diffracted plane waves. Even for $k_\parallel = 0$, there are many resonant standing-wave modes at different frequencies, associated with different zero–group-velocity band edges along the ΓM direction. One such mode, at a frequency corresponding to the $\Sigma 2$ extremum of the second band, is depicted in Fig. 3-7 for $L = 12d$.

We then compute the Q of modes associated with four different band extrema as a function of the cavity size L, and plot the results in Figs. 3-8(a)–3-8(c). (Q is computed using a filter-diagonalization analysis [61] of a finite-difference time-domain simulation [62] implemented in a free software package [63].) In each one of these plots, as discussed above, we might expect to see periodic peaks in Q at intervals of $\Delta L = \pi/k_\perp$, but this will be complicated by the periodicity of the underlying structure (and the corresponding non-uniqueness of $\mathbf{k}$). The simplest behavior occurs for the band extrema $M1$ and $M2$ at the M point $\mathbf{k}a/2\pi = (0.5, 0.5)$, for which $k_\perp = \pi/d$. In this case, since the primary length scale (corresponding to the largest Fourier component $\mathbf{G} = 0$) induces a length scale $\pi/k_\perp = d$ equal to the increment in L, the graphs appear smooth and monotonically increasing as expected

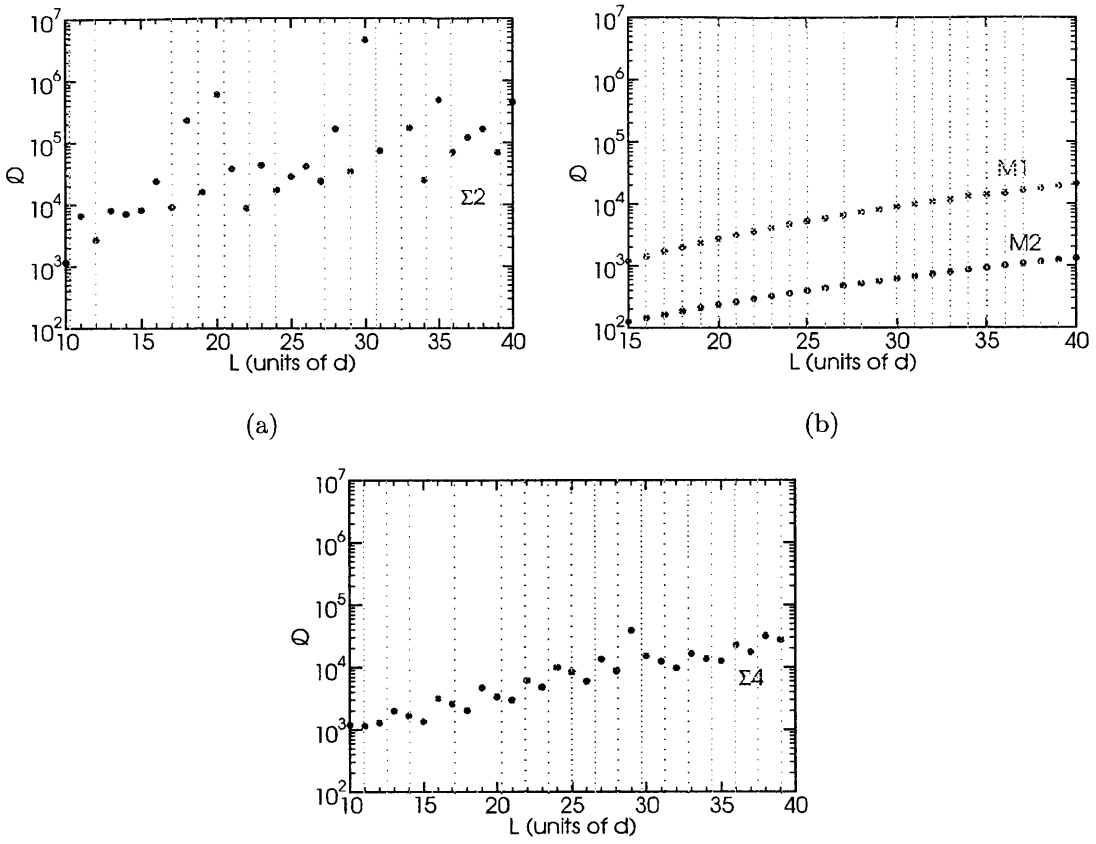

Figure 3-8: Resonant modes of a cavity formed from an finite section of a photonic crystal. The units of length is $d = a/\sqrt{2}$ where a is the lattice constant. The dashed gray lines mark the induced periodicity due to the k point with zero-group velocity. For (a) $\mathbf{k}a/2\pi = (0.293, 0.293)$ at $\Sigma 2$, (b) $\mathbf{k}a/2\pi = (0.5, 0.5)$ at M1 & M2 and (c) $\mathbf{k}a/2\pi = (0.318, 0.318)$ at $\Sigma 4$.

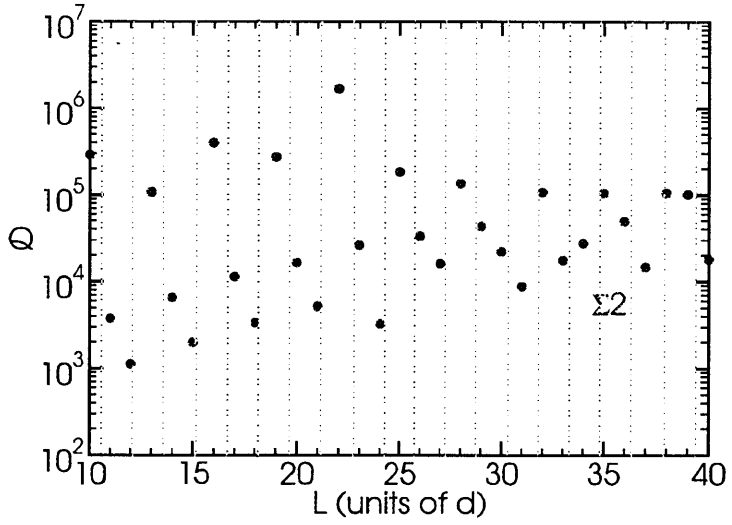

Figure 3-9: The second band minimum is shifted to $\mathbf{k}a/2\pi = (0.33, 0.33)$, which yields the same oscillatory dependence on L seen in the fourth band in Fig. 3-8(c).

from above. In fact, Q goes as L^3. This cubic dependence of the radiative Q on cavity length will be seen again in the context of metallic waveguides in Chapter 5. The most interesting results are shown in Fig. 3-8(a) corresponding to the $\Sigma 2$ extremum, $\mathbf{k}a/2\pi = (0.293, 0.293)$, for which Q exhibits dramatic spikes (increasing by up to two orders of magnitude to $Q \sim 10^6$) at apparently irregular intervals. The ability of $\Sigma 2$ modes to exhibit extremely large Q compared to other band extrema lies in interference between the four modes in the crystal around such an extremum, as discussed further below. The irregularity of the peaks lies in the fact that the induced length scale $\pi/k_\perp = d/0.586$ does not have a small least-common multiple with d. In contrast, consider Fig. 3-8(c), which comes from the $\Sigma 4$ anti-crossing extremum at $\mathbf{k}a/2\pi = (0.318, 0.318)$, which has an induced length scale $\pi/k_\perp$ that is close to $3d/2$, and hence Q displays nearly periodic peaks with period $3d$. The peaks in this case are not nearly so large as for Fig. 3-8(a), as discussed below, because the distinctness of the modes surrounding the extremum inhibits interference effects. To further reinforce our understanding of the Q peaks in Fig. 3-8(a), verifying that they indeed stem from an interference effect associated with $\mathbf{k}$ at the extremum, we examined a slightly modified structure: we tweaked the index contrast to shift the $\Sigma 2$ extremum to $\mathbf{k}a/2\pi = (0.33, 0.33)$. In this case, the induced length scale of the dominant Fourier component is $\pi/k_\perp \approx 3d/2$, and we expect to see periodic Q peaks at intervals of roughly $3d$. This prediction is confirmed in Fig. 3-9, which displays Q vs. L for this tweaked structure. (Q is still not exactly periodic because there are multiple $\mathbf{G}$ components present, but the largest peaks are separated by $\Delta L = 3d$.)

The unusual behavior of the cavity Q in Fig. 3-8(a), with its many sharp peaks, lies in an interference phenomenon: as shown in fig. 3-10, near a band extremum away from the edge of the Brillouin zone we have four modes out of which to build a standing-wave resonance, instead of only two modes as for an ordinary extremum

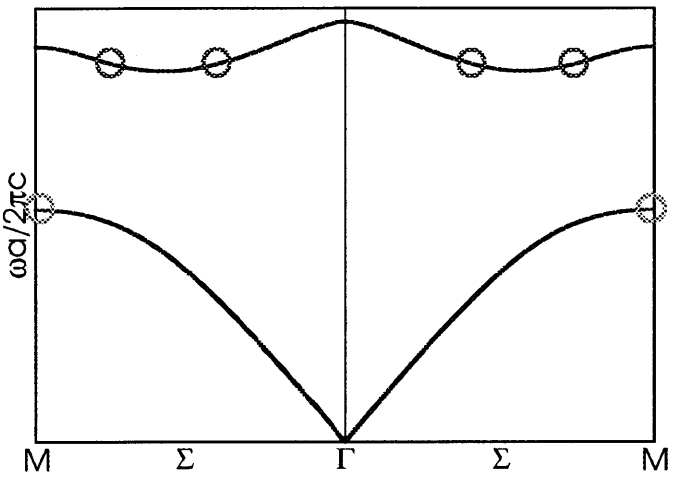

Figure 3-10: Differences in the number of excited modes (circles) for the two cases in Figs. 3-8(a) and 3-8(b).

at the zone edge or center. These four modes, or two pairs of counter-propagating modes, can form a superposition of two standing-wave patterns whose radiative fields destructively interfere, thus increasing Q. This can happen for both the extremum of the second band, where $\eta_{\mathbf{H}}$ changes sign, and for the extremum of the fourth band, where $\eta_{\mathbf{H}}$ does not change sign. But as shown in fig. 3-8(a) the former have much more pronounced peaks in Q than the latter. This difference is directly connected to the change of sign in $\eta_{\mathbf{H}}$! As a general principle, one expects that modes that are more similar will interfere more readily, and hence have larger Q peaks. Perhaps counter-intuitively, the fact that $\eta_{\mathbf{H}}$ changes sign, is an indication that modes just on either side of the extremum in the second band are more *similar* than the corresponding modes for the fourth band where $\eta_{\mathbf{H}}$ does not change sign The reason for this is that $\eta_{\mathbf{H}}$ changes sign only when the Fourier decomposition of the field pattern is *similar* (and hence has a similar "phase velocity") on either side of the extremum despite the change in sign of the group velocity. Hence, the change in sign of $\eta_{\mathbf{H}}$ is correlated to the higher Q peaks for the second band.

In conclusion, it has been shown that a new measure of anomalous behavior, $\eta_{\mathbf{H}}$ determined by the average phase velocity, which was motivated by homogeneous negative-index media, can yield new information differentiating among the zero–group-velocity modes. This characterization of anomalous behavior appears to be independent of the arbitrary choice of norm used to define "average" phase velocity. Zero–group-velocity modes away from high-symmetry points exhibit qualitatively different behavior than zero–group-velocity modes at the band edge, and even among themselves have distinct behaviors depending on the sign of $\eta_{\mathbf{H}}$.

Chapter 4

Optimization of front coatings

4.1 Introduction

Thin film photovoltaic cells are an increasingly attractive route to solar based energy due primarily to reduced material costs. However most of the useful photons for generating the photo-current lie in the infrared where silicon is a poor absorber. Here, I describe efforts to boost the absorption of the long wavelength photons with optimized multiple front coatings.

Front coatings are a critical feature of the highest-efficiency photovoltaic cells, ranging from monocrystalline silicon cells with double-layer anti-reflection (AR) coatings [32] to thin-film CIGS cells with single-layer AR coatings [64]. The most effective front coatings allow light over a broad range of wavelengths to enter the cell and be absorbed. This broad range of wavelengths extends from long-wave ultraviolet (around 300 nm [65]) to the bandgap wavelength (for silicon, 1108 nm [1]). While single-layer front coating designs are well known, multiple layers could conceivably allow higher admittance over a broader bandwidth. The problem of opti-

mizing multilayer coatings for solar cells has been a topic of great interest for some time [66, 67, 68, 69, 70, 71, 72, 73, 74, 75], but the full range of possible designs had not been explored, especially for thin absorbers and/or multiple coatings. Here, we attack this problem with global optimization to find the best possible multilayer film designs in several regimes and quantify the degree of improvement which can be achieved in each case. We show that two front coatings produce the majority of improvement; additional front coatings yield rapidly diminishing improvements. For the most common type of solar cell, made from silicon wafers, the front-coating design problem mostly reduces to a broad-band anti-reflection problem with dispersion. However, due to the dispersion of silicon [1] and the non-uniformity of the AM1.5 solar spectrum [76], this problem can only be solved approximately with an analytical approach [77]. More precise solutions require a numerical approach—Refs. [78, 79, 80] treat the cases of single-layer and double-layer AR coatings; Ref. [81] treats single- through triple-layer AR coatings. Similar approaches have been taken for other related wide-band absorption problems, as in Refs. [82, 83, 84]. Some authors have even expanded this problem to include long wavelengths beyond the bandgap of silicon [75].

On the other hand, emerging thin-film solar cell technology presents an entirely different challenge for front coating design. First of all, reflections from the front and back interfere over a broad range of wavelengths. Furthermore, unlike a narrow bandwidth problem, where the principles of Q-matching resonant absorption (also known as "impedance-matching") can be applied, the portion of the solar spectrum considered is broad-bandwidth, 600 nm to 1100 nm. Moreover the absorption length over the bandwidth is typically greater than the physical optical path length [85]. As a consequence, even light that initially passes through the front coating often reflects back out through the front without being absorbed—an effect not accounted

for in Refs. [78, 80, 81, 86], and [87]. Since the front coatings need to both transmit light and trap it to be absorbed, this increases the complexity of the problem while diminishing the accuracy of any analytical approximations. This was examined through ray tracing on a non-systematic basis for thick multicrystalline wafer-based cells [88, 89]. Some recent work on the opposite limit of extremely thin (15 nm) organic cells has demonstrated 40% boosts in relative efficiency [90] with appropriately designed front coatings. Also, the application of multiple reflections to ultra-thin (5-55 nm) amorphous silicon has been discussed [73].

The behavior of the cell designs depicted in Fig. 4-1, a photovoltaically active silicon region backed by a perfectly reflecting metal region with a varying number of dielectric coatings added to the front and back, is considered. It will be shown that as long as the back reflector consists of low-loss planar layers, its specific design will have negligible impact on the wide-bandwidth problem, though it will have a large impact on the narrow-bandwidth problem. The thicknesses and indices of each front and back coating are chosen by an exhaustive global-optimization procedure to maximize the short-circuit current of each cell.

4.2 Formulation of the problem

The key factor that enables the use of global optimization to exhaustively search the parameter space of possible front-coating films is the availability of extremely efficient algorithms to model the optical properties of multilayer films. In particular, the light-trapping properties of the structures discussed in this paper are studied using a transfer-matrix approach known as the S-matrix method [91, 92]. The structure is broken up into homogeneous slabs of chosen thicknesses, boundary conditions are imposed at the interfaces, and fields are propagated throughout the structure. The

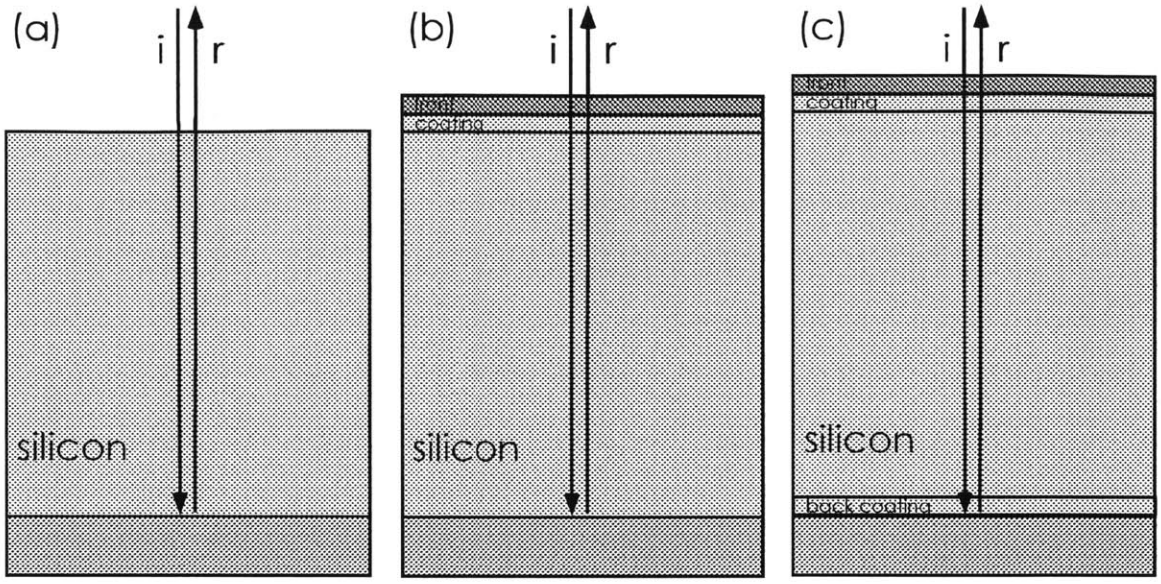

Figure 4-1: Schematic illustration of solar cell designs studied here: (a) a photovoltaically active silicon region (green), backed by a perfectly reflecting metal (gray), (b) diagram (a) with one or more front coating depicted in shades of blue, and (c) diagram (b) with one back dielectric coating layer.

boundary conditions employed in this work correspond to light normally incident from above the solar cell. Light absorption is calculated by modeling the c-Si regions with a complex refractive index that depends on wavelength, as in Ref. [1]. The c-Si region is treated as if it is only intrinsic, i.e., the doping of the p- and n-doped regions can be considered to have a negligible impact on the optical properties of the device. Since most dielectric materials have very large band gaps, the dispersion and absorption of the front and back coatings is assumed to be negligible over the range of wavelengths considered in this work [78]. The metal back-reflector is modeled as a frequency independent, negative permittivity (lossless) medium (as shown later, the exact details of the back-reflector have almost no impact on the optimal front coating design for the full solar bandwidth problem). In principle, the calculation of the model's optical properties is exact apart from these approximations. Verification

has been performed for several structures using the finite-difference time-domain method [93] with perfectly-matched boundary layers [94]. While the results are in good agreement, the FDTD method is much slower for the same level of accuracy, so it is not used for the reminder of the calculations.

In order to calculate the efficiency of the light capture of the model it is assumed that each absorbed photon with energy greater than the band gap energy generates an electron-hole pair, and both carriers reach the electrical contacts. This corresponds to the statement that the diffusion length L_D is much greater than the distance traveled by each carrier (i.e., $L_D \gg d$), a reasonable assumption for thin Si films with high mobilities.

The optimized quantity is the generated short-circuit current J_{sc}, given by [95]:

$$J_{sc} = \int d\lambda \left[\frac{e\lambda}{hc} \frac{dI}{d\lambda} A(\lambda) \right] \equiv \int d\lambda \, w(\lambda) A(\lambda) \tag{4.1}$$

where $\frac{dI}{d\lambda}$ represents the light intensity experienced by the solar cell per unit wavelength (given by the ASTM AM1.5 solar spectrum [76]), and $A(\lambda)$ is the absorption calculated above. (The integration was carried out by a 1000-point trapezoidal rule.) The coefficients $w(\lambda)$ capture the relative importance of absorption at each wavelength, and will be referred to as "current weights" for short. This allows us to define a figure of merit (FOM) by:

$$\text{FOM} = \frac{\int d\lambda \, w(\lambda) A(\lambda)}{\int d\lambda \, w(\lambda)} \tag{4.2}$$

which is proportional to the objective function we wish to maximize. It gives us a measure of the absorbing efficiency of the structure weighted for the solar-cell application; perfect absorption at all wavelengths within the range of silicon's absorption

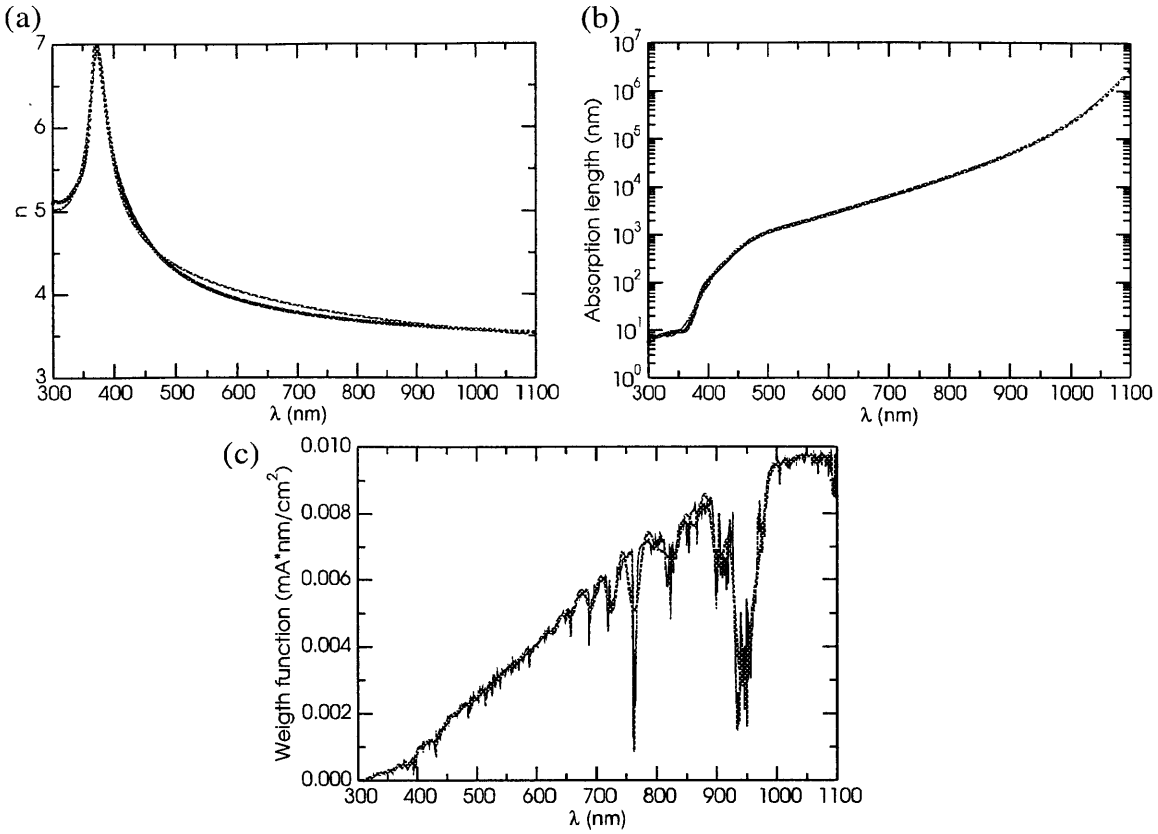

Figure 4-2: Fits of calculation parameters (red curves) to actual data derived from references (blue curves): (a) real index of crystalline silicon [1] (b) absorption length of crystalline silicon [1] (c) current weights $w(\lambda)$ in Eq. (4.1), fit with a degree-100 Chebyshev approximation [2].

(300 nm to 1108 nm) yields FOM $=$ 1.

Important spectra factoring into the J_{sc} calculation are displayed in Fig. 4-2: the real indices and absorption lengths of silicon, and current weights $w(\lambda)$. In each plot, the experimental data is shown in blue, while the smooth fit used to calculate the results in the following section is shown in red. For the case of the real index of silicon, a Lorentzian plus a polynomial fits the data well. Since the absorption length grows exponentially with wavelength, a polynomial fit was made

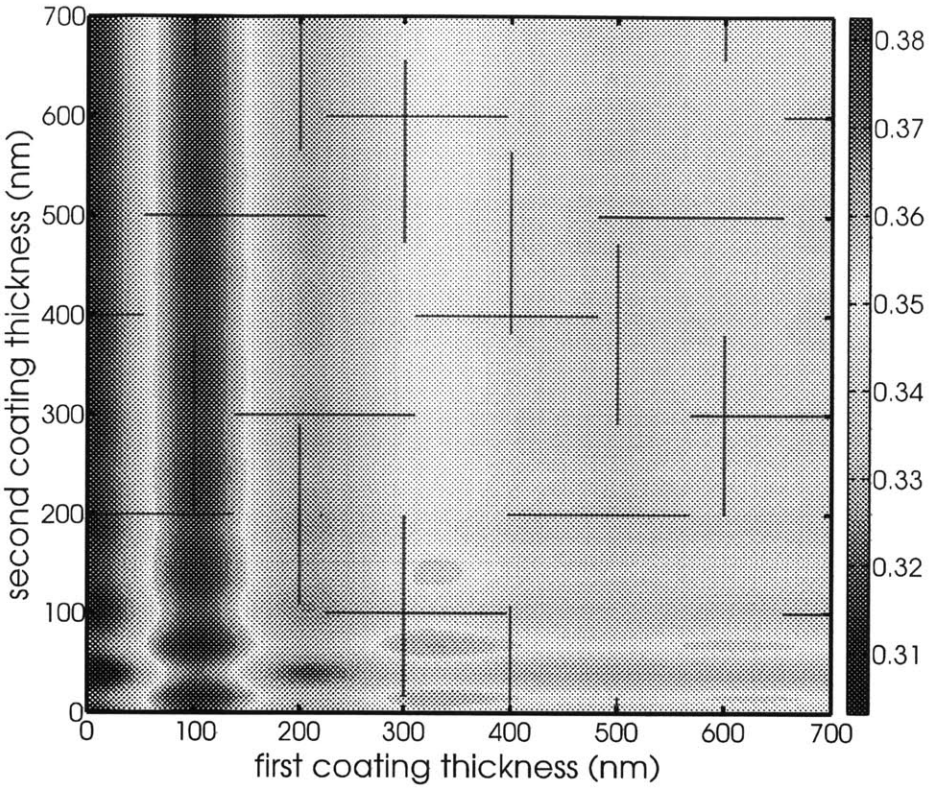

Figure 4-3: A contour plot of the FOM of a cell with two front-coating layers versus the layer thicknesses (the indices of each layer are fixed at 1.27 and 4.35). The FOM ranges from 0.30 (blue) to 0.38 (red). The presence of many local optima necessitates a global optimization approach.

to the logarithm of the imaginary part of the index. Finally, the current weighting function $w(\lambda)$ in Eq. (4.1), which is based on the AM1.5 solar spectrum [76], was fit with a degree-100 Chebyshev approximation, which displays more stability than its standard polynomial counterpart [2].

For the calculations, the front coating thicknesses were bounded by 0 nm and 700 nm and the indices by 1 and 5. The range of thicknesses includes the largest quarter-wave thickness in the lowest index material; the range of indices includes most materials that can be easily fabricated as a front coating. However, as discussed

at the end of Section 1.3, restricting the range of indices to a narrower range, or even fixing the indices entirely to the values for selected materials and optimizing only over the thicknesses, yields a FOM only slightly lower than when a wide range of indices is explored.

In general, this problem may have many local optima, especially as the range and number of parameters are increased. This is illustrated in Fig. 4-3, which plots the FOM as a function of two of the four parameters (two coating thicknesses) and exhibits many local optima. To avoid these suboptimal solutions, we apply a global optimization technique that exhaustively finds all local optima and picks the best one. In particular, we employ the MLSL algorithm [96], which combines efficient local search (we used the limited-memory BFGS algorithm [97] with an open-source implementation[98]) with quasi-random starting points based on a Sobol low-discrepancy sequence [99, 100, 101]. The MLSL algorithm is distinguished by clustering techniques to avoid repeatedly searching the same local optimum, and is guaranteed to find all local optima in a finite number of local searches [96]. We also compared MLSL to several other global-optimization techniques, such as the DIRECT-L algorithm [102], via a free-software package implementing many optimization algorithms [103], and found MLSL to find the same optimum in a shorter time. Because the BFGS algorithm requires the gradient of the objective function (the FOM), a computationally efficient method for calculating the gradient based on the adjoint method was used. Adjoint methods allow the gradient to be computed in a time comparable to the time required in calculating the objective function and independent of the number of parameters [104].

4.3 Results and discussion

In order to understand the physically-relevant problem of maximizing short-circuit current in a solar cell subject to the AM1.5 solar spectrum, it is instructive to start at the simpler, opposite limit of zero bandwidth. In this zero-bandwidth limit, it is well known that 100% absorption can be achieved when the rate of radiative escape from a resonant cavity is equal to its rate of absorption [5, 105]; this is referred to as the Q-matching condition. Thus, it is predicted that the optimal design of Fig. 4-1 with an arbitrary number of front layers should be capable of reaching 100% absorption at any given wavelength, simply by employing a periodic Bragg-mirror structure to confine the light at that wavelength with the appropriate lifetime. For a bounded number of layers, on the other hand, 100% absorption should only be reached up to a certain wavelength λ_t, since for $\lambda > \lambda_t$ the absorption will be too small (corresponding to a high absorptive Q that cannot be matched by a small number of layers). Thus, the value of λ_t will be determined by the maximum possible value of the radiative Q achievable for a fixed number of front-coating layers and a fixed range of indices. The absorption and radiative Q must be large enough in order for it to be accurately described by a resonance process, the absorption length must be much larger than the silicon thickness, and the light must be trapped for a time much larger than the period. For instance, consider a front coating design of a 3 layer quarter–wave stack. The absorption Q, due to the silicon layer with complex index of refraction $n(\lambda) + \imath\kappa(\lambda)$, is $n(\lambda)/\kappa(\lambda)$. The radiative Q of the quarter–wave stack is,

$$Q = \frac{4\pi t n(\lambda)}{\lambda} \frac{\sqrt{R}}{1-R} \tag{4.3}$$

where $n(\lambda)$ is silicon's real index, t is the silicon layer thickness, and the reflectance of the quarter–wave stack given by

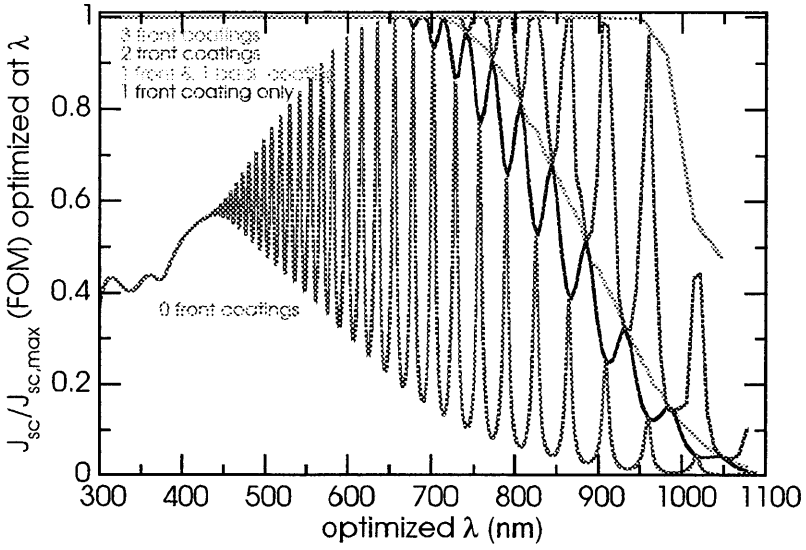

Figure 4-4: The generated current efficiency as a function of wavelength; the parameters for each structure class (e.g., two front layers) are optimized separately at each wavelength i.e., this is the reflection spectrum for many different structures. Note that structures with one or more front layers display full absorption up to a particular wavelength λ_t that increases with the number of front layers.

$$R = \left| \frac{1 - n(\lambda)\,(n_2/n_1)^3}{1 + n(\lambda)\,(n_2/n_1)^3} \right|^2 \tag{4.4}$$

where n_1 and n_2 refer to the indices of the layers. It found that for $\lambda_t > 1000.2$ nm the absorption Q is too large and Q-matching becomes impossible for the 3-layer quarter–wave stack.

This prediction is tested numerically using the simulation framework discussed in the previous section; the results are shown in Fig. 4-4. For zero front coating layers, the large dielectric contrast between silicon and air allows effective transmission at only a handful of wavelengths (due to destructive interference of the reflected wave).

For a single front coating, the absorption is given by $A = 1 - |r|^2$, where:

$$r = -\frac{e^{i\phi_2}(e^{i\phi_1} + r_1 r_2) + r_2 e^{i\phi_1} + r_1}{e^{i\phi_2}(r_1 e^{i\phi_1} + r_2) + r_1 r_2 e^{i\phi_1} + 1} \tag{4.5}$$

where layer 0 is air, layer 1 is the front coating, and layer 2 is the silicon; n_j is the real part of the refractive index of layer j, κ_j is the imaginary part, t_j is the thickness, λ the vacuum wavelength. At normal incidence, $\phi_j = 4\pi(n_j + i\kappa_j)t_j/\lambda$ and $r_j = (n_j + i\kappa_j - n_{j-1} - i\kappa_{j-1})/(n_j + i\kappa_j + n_{j-1} + i\kappa_{j-1})$ are the phases and Fresnel reflection coefficients[106].

The reflectivity can be divided into three regimes, depending on the fractional absorptance of the silicon layer:

- $|e^{i\phi_2}| \ll r_2$: here, virtually no light reaches the back reflector. Thus, the problem reduces to that of creating an anti-reflection coating between two semi-infinite regions, as discussed in Ref. [106]. The reflection is now written as $r \approx -(r_2 e^{i\phi_1} + r_1)/(r_1 r_2 e^{i\phi_1} + 1)$. With the proper choice of front-coating layer index and thickness, 100% transmission (and thus, 100% absorption), can be achieved at a single λ [106]. This is exhibited by our results up to a wavelength of 575 nm in Fig. 4-4; for wavelengths between 575 and 700 nm complete absorption is instead due to Q-matching.

- $|e^{i\phi_2}| \approx r_2$: here, partial absorption after one pass through the cell means that interference between reflections from the front and back surfaces is possible. Furthermore, it is impossible to fully optimize this system by controlling a single, uniform dielectric layer. Mathematically, solving for the root of the numerator of Eq. (4.5) requires three independent variables because it has four linearly independent terms. If only two independent variables are present, a constant value is added to a term which rotates in the complex plane. This

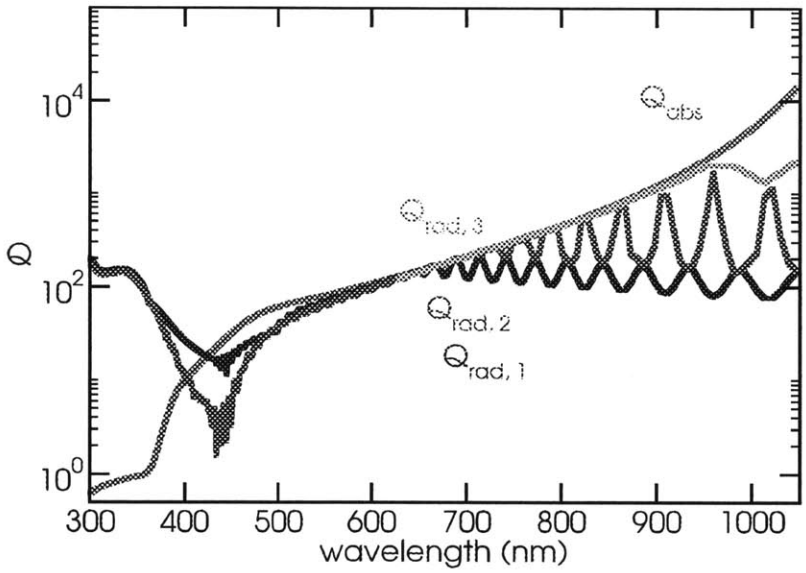

Figure 4-5: The absorptive Q (magenta) and the radiative Q of 1,2, and 3 front coatings versus wavelength. Below 550 nm Q-matching is unnecessary, since the absorption length is equal to or less than the silicon layer thickness, and absorption is due to an anti-reflection coating.

results in Fabry-Perot-type oscillations, which are seen in Fig. 4-4 for wavelengths ranging from 675 to 1050 nm. However, these Fabry-Perot oscillations can be suppressed with an additional single back layer, illustrated in Fig. 4-1(c), which shifts the Fabry-Perot oscillations of the silicon slab to a maximum at each λ. To enhance light-trapping at wavelengths where the absorption length of silicon is large, the optimal index of the front coating is the maximum allowed value. Because of the π-phase shift from this layer, the Fabry-Perot peaks are shifted by half a period with respect to the zero front-coating FOM. This trend continues with the two front-coating FOM, there are two π-phase shifts realigning the peaks with the zero front-coating FOM. Finally, note that the onset of these oscillations is red-shifted as the number of front coatings increases, from 675 nm for one front layer, up to 725 nm for two front layers, and 950 nm for three front coatings due to improved light-trapping with an increase in the number of front coatings, as predicted above. Note that this is consistent with where the radiative Q begins to deviate from the absorptive Q in Fig. 4-5.

- $|e^{i\phi_2}| \rightarrow 1$: here, the absorption strength is virtually nil, and Q-matching cannot be achieved without a number of front layers proportional to $|\log(1 - |e^{i\phi_2}|)|$, since the maximum radiative Q grows exponentially with the number of layers [5]. Mathematically, the amplitude of the reflection coefficient $|r|$ will approach unity. This limit is approached on the right-hand side of Fig. 4-4.

Next, consider what happens to the FOM as the window of absorption wavelengths expands from zero up to the width of the usable solar spectrum for silicon-based solar cells (300–1108 nm). The results for optimized structures with 0–3 front layers are plotted in Fig. 4-6; three distinct bandwidth regimes can be seen. First, the

smallest bandwidths (below 1 nm) are similar to the zero bandwidth problem plotted in Fig. 4-4, for λ =902.8 nm. Since the absorption length of silicon at λ =902.8 nm is about 50 μm, several front layers are necessary to increase the radiative Q for Q-matching to be achieved. Second, it is evident that Q-matching starts to break down for bandwidths greater than 1 nm. That is because Q-matching relies on the accuracy of coupled-mode theory, which assumes a narrow-bandwidth cavity (i.e., one that is weakly coupled to losses so that its decay rate is long compared to the optical period) [5]. When that assumption is violated, it is no longer possible to achieve 100% absorption over the entire bandwidth; the severity of the violation dictates the extent of the decrease in the average absorption. Third, the increase in the FOM for large bandwidths (above 265 nm) demonstrate that absorption can be boosted by blue-shifting the central wavelength and adding in more wavelengths for which even a thin film is optically thick.

Now let us consider the problem of absorption over the whole solar spectrum in more detail. The absorption spectra of optimized thin-film crystalline silicon solar cells ($t = 2\,\mu$m) are plotted in Fig. 4-7 for structures with no front layers [based on Fig. 4-1(a)] as well as optimized structures with 1–3 front layers [based on Fig. 4-1(b)]. It is evident that the optimal design employs a peak absorption around 450 nm, which represents a trade off between the shorter absorption lengths at smaller wavelengths [illustrated in Fig. 4-2(a)] and the greater current weights at longer wavelengths [illustrated in Fig. 4-2(b)].

The values of the front coating indices, thicknesses and figure of merit for the optimized structures of Fig. 4-7 are listed in Table 4.1. The layers slowly increase in index towards the silicon layer, consistent with the intuition that a front layer with a smoothly increasing index profile would allow 100% transmission to the silicon layer. (The optimal front coating is *not* a total transmission AR coating, however, be-

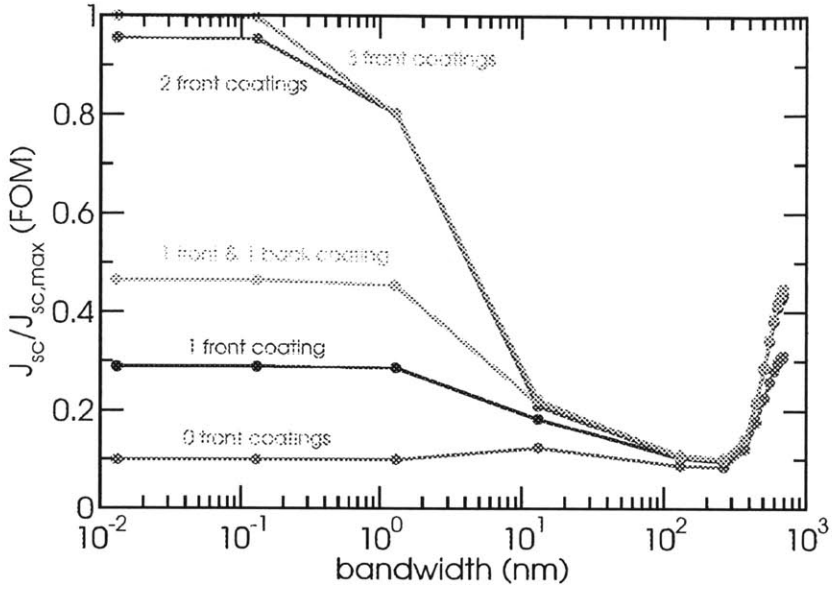

Figure 4-6: The generated current efficiency versus the bandwidth of incoming radiation; for bandwidths up to 265 nm the central wavelength is 902.8 nm, for bandwidths above 265 nm, the maximum wavelength is fixed, while the minimum wavelength is decreased (which corresponds to a blue shift of the central wavelength).

Table 4.1: Table of optimized front-coating designs for one, two, and three front-coating layers, as in Fig. 4-1(b). Layers are ordered from closest to air. Coating thickness d in units of nm.

Number of front coating layers	1		2		3	
Figure of merit	0.439		0.455		0.458	
Layer indices and thicknesses	n	d	n	d	n	d
	2.08	60.0	1.54	82.3	1.34	91.0
			3.02	38.9	2.39	53.1
					3.79	29.9

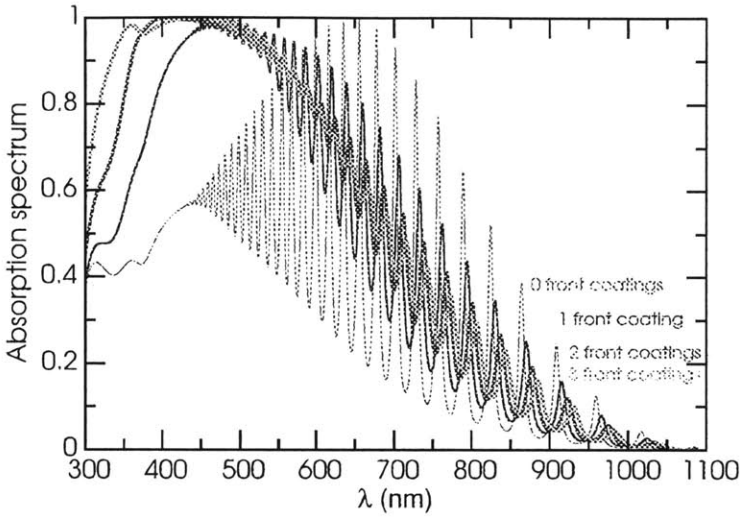

(a)

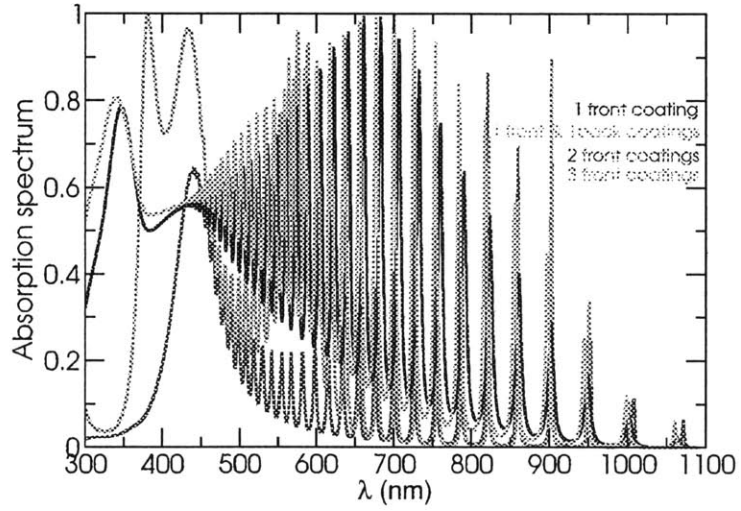

(b)

Figure 4-7: Absorption spectrum over the full absorbing bandwidth for a thin-film crystalline silicon solar cell ($t = 2\mu$m). (a) Optimized over the full bandwidth and (b) optimized only at $\lambda = 902.8$ nm.

cause it must act as a partially silvered mirror, particularly in the narrow-bandwidth limit). Moreover, as one might expect, each of the optimized front coatings generates destructive interference between reflections from their front and back at the central frequency (corresponding to a phase shift $\approx \pi$). In addition, the optimized structure for the 1 front-coating and 1 back-coating structure was found to be $d = 60.0$ nm, $n = 2.070$ and $d = 20.7$ nm, $n = 1$, respectively; the corresponding figure of merit was 0.440, which is nearly the same as the 1 front-layer structure. While it appears that the back coating is not of much use in a broad bandwidth problem, for a lossy metallic back reflector the back coating can help to reduce unwanted absorption loss.

Let us consider the effects of thickness over a broad range of silicon thicknesses, from thin-film values of 1 μm to effectively semi-infinite values of 1.6 cm. For the case of 2 μm-thick thin films, increasing the number of front coatings from zero to one yields a relative increase of 39.8% to the FOM (from 0.314 to 0.439); adding a second front coating yields a relative increase of 3.6% to the FOM (to 0.455), and adding a third coating yields another relative increase of 0.6% (to 0.458). For wafer-based cell thicknesses, e.g., 256 μm, increasing the number of front coatings from zero to one yields a 42.3% relative increase in the FOM (from 0.614 to 0.874); adding a second coating yields a relative increase of 6.1% (to 0.927); adding a third coating yields a relative increase of 1.3%. For effectively semi-infinite cells, e.g., 1.6 cm, increasing the number of front coatings from zero to one yields a 42.0% relative increase to the FOM (from 0.645 to 0.916); adding a second coating yields a 6.6% relative increase (to 0.976); and adding a third coating yields a relative increase of 1.5% (to 0.991).

These numbers illustrate the diminishing returns associated with adding more front layers for the broad-bandwidth problem. Thus, it is no surprise that increasing the number of layers to 10 provides no more than a 0.9% relative improvement over 3 layers, for a 2 μm-thick thin film. This result contrasts strongly with the zero-

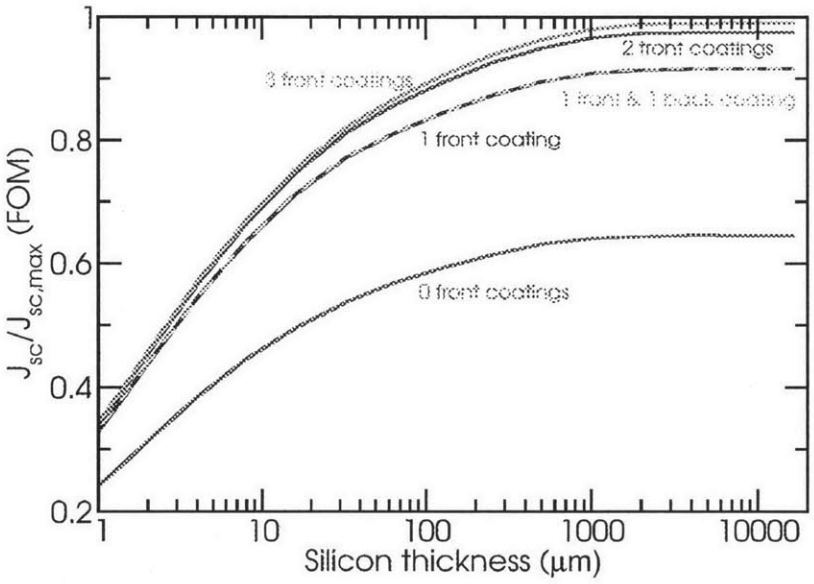

Figure 4-8: Figure of merit versus silicon slab thickness, both for a structure with no front layer (based on Fig. 4-1(a)) and optimized structures with 1-3 front layers (based on Fig. 4-1(b)).

bandwidth results shown in Fig. 4-4, where each additional layer results in a large improvement (up to the critical number required for Q-matching). As discussed previously, this crossover occurs in the intermediate bandwidth regime (1-265 nm), as illustrated in Fig. 4-6. Furthermore, the relative and absolute gains are greater for the thicker, wafer-based cells than for thin films. This can be explained by noting that the long wavelengths that are poorly absorbed by thin cells with a single front coating layer can be absorbed well by thick cells. Thin-film cells are simply too thin to ever strongly absorb longer wavelengths without compromising their shorter-wavelength absorption, whereas wafer-based cells are free from this limitation. This assertion is also supported by the absorption spectra of Fig. 4-7, in which the optimal designs display increasing absorption with the number of front coatings primarily at shorter wavelengths.

For thin films exposed to the full solar bandwidth, the FOM and the optimal front-coating design are insensitive to the type of back-reflector. Considering only lossless planar back-reflectors and limiting ourselves to completely specular reflection, different back-reflector schemes (different materials, Bragg mirrors, etc.) are distinguished only by the phase θ of the reflected wave. However, we show here that the FOM is essentially independent of the back-reflector phase. Of course, this phase generally varies with wavelength, but it is sufficient to demonstrate this independence using a constant phase (employing $n = 3.5$ for silicon and a constant imaginary index for the back-reflector, as explained previously). The FOM relative difference, which measures the influence of the back-reflector on the absorption, versus θ is shown in Fig. 4-9. For each back reflector, the FOM must be calculated twice, once with the optimal front coating design for that particular back reflector and again with the optimal front coating design of the original back reflector ($\theta = 0$). We find the relative difference to be very small, less than 0.0001 for the single front-coating structure.

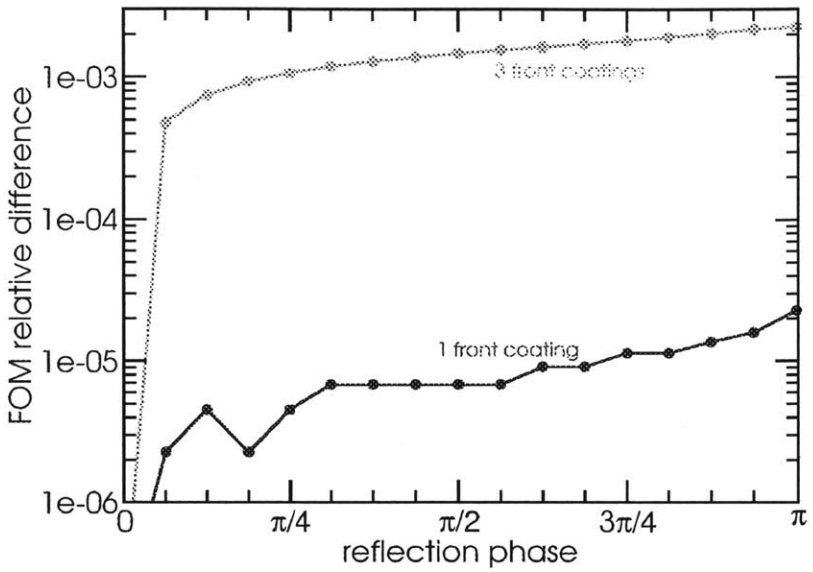

Figure 4-9: Relative difference in figure of merit, calculated as the relative difference of the FOM for the optimized structure with the given reflection phase and the FOM of a structure with the given phase and with the optimized front coating of the reference phase ($\theta = 0$), versus the Fresnel reflection amplitude phase of the silicon-metal boundary.

This robust behavior is enabled by the large bandwidth of the incident flux that averages out the change at each λ; while the location of the absorption peaks can shift, the total absorbed flux will show almost no change as illustrated in Fig. 4-10. Therefore, metallic backings where absorptive losses are present, such as aluminum, can be replaced with a lossless backing, such as a 1D Bragg mirror.

Though the refractive index bounds exceed those of common materials, we find that optimization with a smaller range of indices, 1 to 3, does not significantly change the FOM. In fact with a restricted refractive index range, the 3 front-coating structure FOM decreases by less than 0.5% (0.458 to 0.456). (The thicknesses and

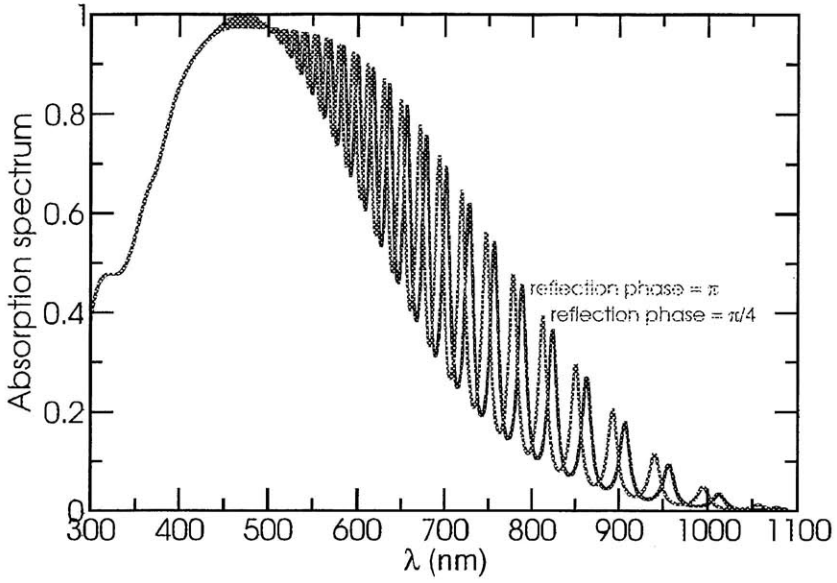

Figure 4-10: Absorption spectrum of the optimized single front coating reference structure for two different back-reflector phases, $\pi/4$ (blue) and π (red). The back-reflector simply shifts the peaks, but has a only negligible effect on the integrated absorption or the FOM.

indices of each layer of the optimal structure changes, including those in the original structure with an index less than 3.) Moreover, if the indices of the front coatings were fixed to values corresponding to experimentally accessible materials and allow only the thicknesses to vary, we find very little change in the FOM, less than a 0.2% relative change in all three cases. If the front coatings were chosen to be MgF_2, ZrO_2, and TiO_2 with indices 1.38, 2.39, and 3.9 yields a FOM of 0.457, a relative decrease of just 0.2% compared to the optimal 3 front-coating structure in Table 4.1. These specific materials are insulators with large electronic bandgaps, and therefore exhibit negligible absorption over the solar bandwidth considered. The Kramers-

Kronig relation predicts that the real index must have very small dispersion as well; for example, the real index of MgF_2 ranges from 1.380 at $\lambda = 825$ nm to 1.398 at $\lambda = 300$ nm.

The designs presented in this work are also robust against small fabrication errors. For example, vertical LPCVD systems can routinely achieve uniformities of better than 2% in the deposition of silicon nitride [107]. For our designs, that corresponds to an error of ± 2 nm or less. However, it's clear that this corresponds to a variation in the objective function of less than 0.001, which shows that our designs can tolerate typical experimental errors.

4.4 Conclusions and future work

In conclusion, the proper design and optimization of front coatings of crystalline silicon solar cells has a critical impact on their overall efficiency. For narrow bandwidths in optically thin absorbing media, it is best to employ the Q-matching condition. The benefit of additional layers is large until this criterion is achieved. When the bandwidth is equal to the portion of the solar spectrum that can be absorbed by crystalline silicon, it is necessary to take a different approach. It is found that just two optimized layers suffice to realize most of the benefits of a multilayer front coating design. The relative improvement associated with going from one to two front layers is 6.1% for 256 micron-thick wafer-based cells, and only 3.6% for 2 micron-thick thin-film cells. This result comes about because weak absorption of near-IR by planar thin films limits the utility of broadening the bandwidth of strong transmission through the front coating. Adding a third layer yields relative improvements of 1.3% and 0.6% for wafers and thin films, respectively; the results for four or more layers show even smaller additional improvements. The broad bandwidth results achieved do not

depend on the type of back-reflector used.

Though the effect of non-radiative recombination was neglected here, it can be simply incorporated for thin-film cells just by multiplying the short-circuit current with a pre-factor that is independent of the front-coating design. That is because in a thin-film solar cell geometry, the ratio between the contact spacing and the cell thickness is generally 1000:1 or greater. As a result, the system can be treated in a quasi-2D approximation, allowing the charge collection efficiency to be treated independently of the front-coating design. For example, one could construct a model of contact strips spaced by a distance D with a minority carrier collection probability $P_c = e^{-|y|/L_D}$, where y is the distance of the electron-hole pair generation from the nearest contact, and L_D is the minority carrier diffusion length (the diffusion length for majority carriers is infinite by assumption). Spatial averaging yields an overall pre-factor of $(2L_D/D)[1 - e^{-D/2L_D}]$. For a minority carrier diffusion length of 10 mm and a contact spacing of 1 mm the pre-factor is 97.5%. Radiative recombination can be calculated following the approach outlined in Ref. [33]. Under short-circuit conditions, the radiative recombination current cancels with the thermal current, leaving only the J_{sc} term.

The results outlined in this work provide a clear baseline to which more complex, non-planar photonic structures ought to be compared. Future work should address the weak absorption of near-IR by thin-film cells by optimizing 2D or 3D patterns introduced in the front or back coatings, whose purpose is to convert incoming normal incidence radiation to transversely propagating, waveguided modes that achieve a longer optical path within the absorbing layer. Ref. [95] demonstrates how photonic crystals can improve reflection off of a realistic, lossy metal (such as aluminum) while also redirecting light in the near-IR into guided modes. However, periodic patterning has its greatest impact near the diffraction limit where the density of guided

modes is largest. One can also consider the impact of a random surface, in particular correlated roughness. Such a surface profile would resemble some incoherent superposition of multiple gratings and conceivably created more guided modes that enhance absorption. The random and periodic patterning should also enable front coatings to improve absorption over a broader wavelength range than would be possible in a planar structure. This combined approach may result in efficiency gains equal to the sum of their contributions. Finally it may also be beneficial to consider the effect of non-normally incident radiation, one could maximize the performance over a range of incident angles [85].

Chapter 5

Tailoring thermal emission via Q-matching of photonic crystal resonances

A rigorous framework for analyzing the emissivity spectrum of a 2D metallic photonic crystal via coupled-mode theory is constructed. Applying the Q-matching condition to resonant modes allows one to tailor the spectrum to display high emissivity over a specified range of wavelengths; this is verified with finite-difference time-domain simulations. This approach is used to explore a frequency selective emitter for thermophotovoltaics as well as an incandescent lighting element.

5.1 Introduction

The spectral emissivity of a blackbody is unity for all frequencies and is the upper limit that any material can achieve. However, in certain applications it is desirable

to have instead an emitter that radiates only within a certain frequency bandwidth, a selective emitter. Photonic crystals, metallo-dielectric structures with periodic wavelength-scale refractive index modulations, are well-suited for creating a selective emitter by virtue of possessing photonic bandgaps [3, 4, 5, 108, 109]. The addition of metal introduces more flexibility in creating a selective emitter; below the plasma frequency of the metal, electromagnetic fields are strongly attenuated [110, 111], which allows broadband frequency selectivity [110, 111, 112, 113, 114, 115, 116, 117, 118]. However, the high infrared reflectivity of metals implies via Kirchhoff's law [119], a low emissivity and therefore requires a modification of the surface, for example by a 1D array of grooves [112] or a 2D array of holes [113, 114, 115, 116], to suppress reflection at those frequencies. The surface periodicity allows light to couple to diffracted plane waves or surface plasmon-polaritons, if they are present. Moreover if the grooves or holes are large enough they will support waveguide resonances that couple to one another providing another mechanism for enhancing thermal emission by increasing the interaction time of light with the material. While previous work [112, 113, 114, 115] has demonstrated that the resonant peaks due to waveguide resonances occur at frequencies corresponding to the isolated waveguide resonant frequencies, the mechanism and quantitative prediction for the amplitude of the peaks was missing. Here we show that matching the radiative and absorptive rate of the photonic crystal resonances dictates the emissivity spectrum. By tuning a small number of geometrical parameters, tailoring a broadband, selective thermal emitter becomes possible.

In particular, one such application of a selective broadband emitter is in thermophotovoltaics (TPV). In TPV, the emitter, such as a slab of tungsten, is heated to a high temperature and radiates the majority of its energy in the infrared and onto a photovoltaic (PV) cell with a bandgap designed to lie in the infrared [120, 121].

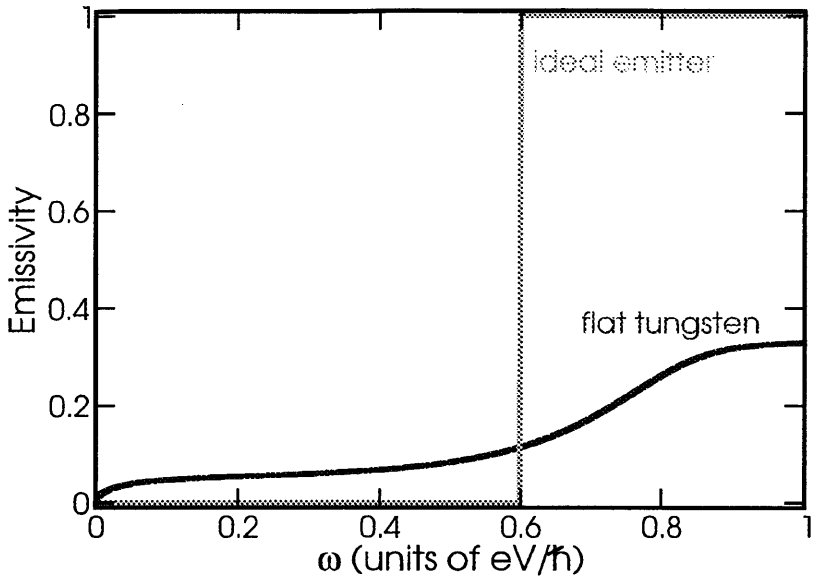

Figure 5-1: Emissivity spectrum of flat, bulk tungsten (blue) and of an ideal selective emitter (green) designed to match the 0.6 eV/$\hbar$ bandgap of InGaAs.

InGaAs, for example, possesses a bandgap of 0.6 eV/$\hbar$ [114, 122]. However, a low efficiency and power density results since the typical greybody has too low emissivity in the infrared; this is remedied with the selective emitter as we'll see.

5.2 Loss rates of waveguide resonances

Consider the emissivity spectra illustrated in Fig. 5-1. The ideal selective emitter should emit only photons with frequency above a cutoff frequency. Here, the cutoff frequency corresponds to the electronic bandgap of InGaAs. Tungsten, chosen here because of its high melting point and low emissivity beyond the cutoff frequency, falls far short of being an ideal selective emitter. However, upon introduction of a

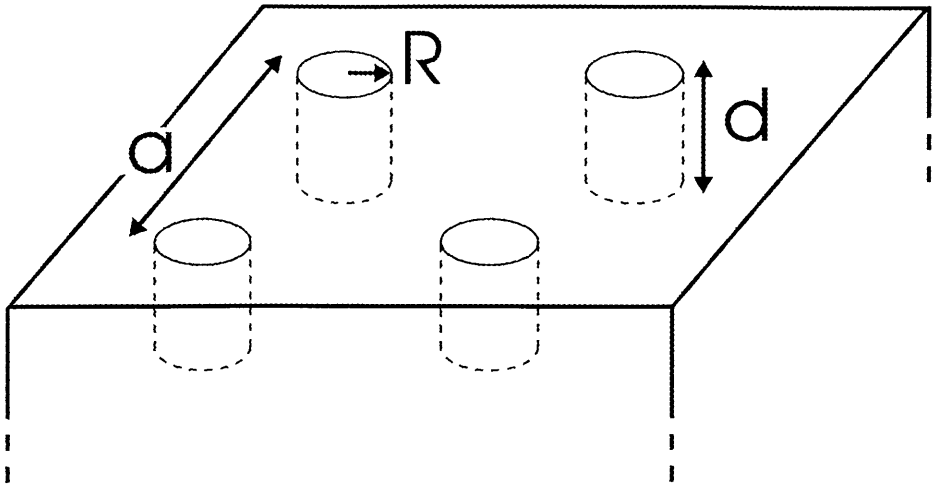

Figure 5-2: A periodic array of cylindrical holes with period a, depth d, and radius R etched into a slab of tungsten. The hole depth is less than the tungsten slab thickness.

periodic array of holes, illustrated in Fig. 5-2, its selectivity can vastly improve via the creation of extra states on the surface that couple to external radiation.

Since the radiative and absorptive rate of these coupled waveguide resonances depend much more strongly on the hole radius R and depth d than on the period a, consider first a single, isolated hole ($a \rightarrow \infty$). Because the field can penetrate into tungsten, the resonant mode within an isolated hole will be a linear combination of HE and EH-like modes. Only resonances with angular number $\nu = 1$ will be considered since only they will couple to normally incident plane waves in a periodic array of holes. In addition, for the R and d values considered here for Q-matching, $\nu = 1$ yields the lowest resonances. The hole resonances experience three types of losses; radiation through the top, absorption on the side walls and bottom, and absorption on the front tungsten surface. The first and second loss mechanisms contribute much more to the total loss rate than the last mechanism, so it is neglected.

If the two remaining loss rates are not too large compared to the resonant frequency, then each can be calculated in the absence of the other [123]. For each loss mechanism a quality factor $Q = \omega_o \tau/2$ is calculated, where ω_o is the resonant mode frequency and τ the lifetime (or inverse loss rate) associated with it. (The quality factor is a dimensionless lifetime: after Q periods a resonance decays by $\exp(-\pi)$.) When these two loss rates are equal– the Q-matching condition– complete absorption of incident radiation occurs.

The loss rate due to absorption can be obtained by closing the top with a perfectly conducting metal. A perfect magnetic conductor cover, corresponding to a electric field maximum at the opening, could just as well be employed since the absorptive rate does not depend much on which boundary condition is used. Finite-difference time-domain (FDTD) simulation is used to simulate the structure [62, 124]. A point source is placed in the cavity, and resonant modes are excited whose loss rates are extracted by a filter-diagonalization method [61]. The resonant frequency $\omega_o a/2\pi c$ and absorptive quality factor $Q_{\text{abs}} = \omega_o \tau_{\text{abs}}/2$ are plotted in Fig. 5-3(a) and Fig. 5-3(b) as functions of R and d for the first three hole resonances. The general trend of Q_{abs} decreasing toward the left can be understood from an equivalent definition of Q, $Q_{\text{abs}} = \omega_o U/P_{\text{abs}}$. Decreasing the hole volume reduces the total field energy U of the mode and forces a larger value of the electric field on the tungsten surface thereby raising P_{abs}. The power absorbed on the bottom increases with the wavevector in the z-direction, hence Q_{abs} decreases with the mode order.

The radiative quality factor $Q_{\text{rad}} = \omega_o \tau_{\text{rad}}/2$, plotted in Fig. 5-3(c), is obtained by replacing tungsten with a perfect conductor in simulations. The lack of an intrinsic length scale implies that Q_{rad} will depend only on the ratio d/R and is manifested in Fig. 5-3(c) as lines emanating from the origin. To leading order in d/R it can be

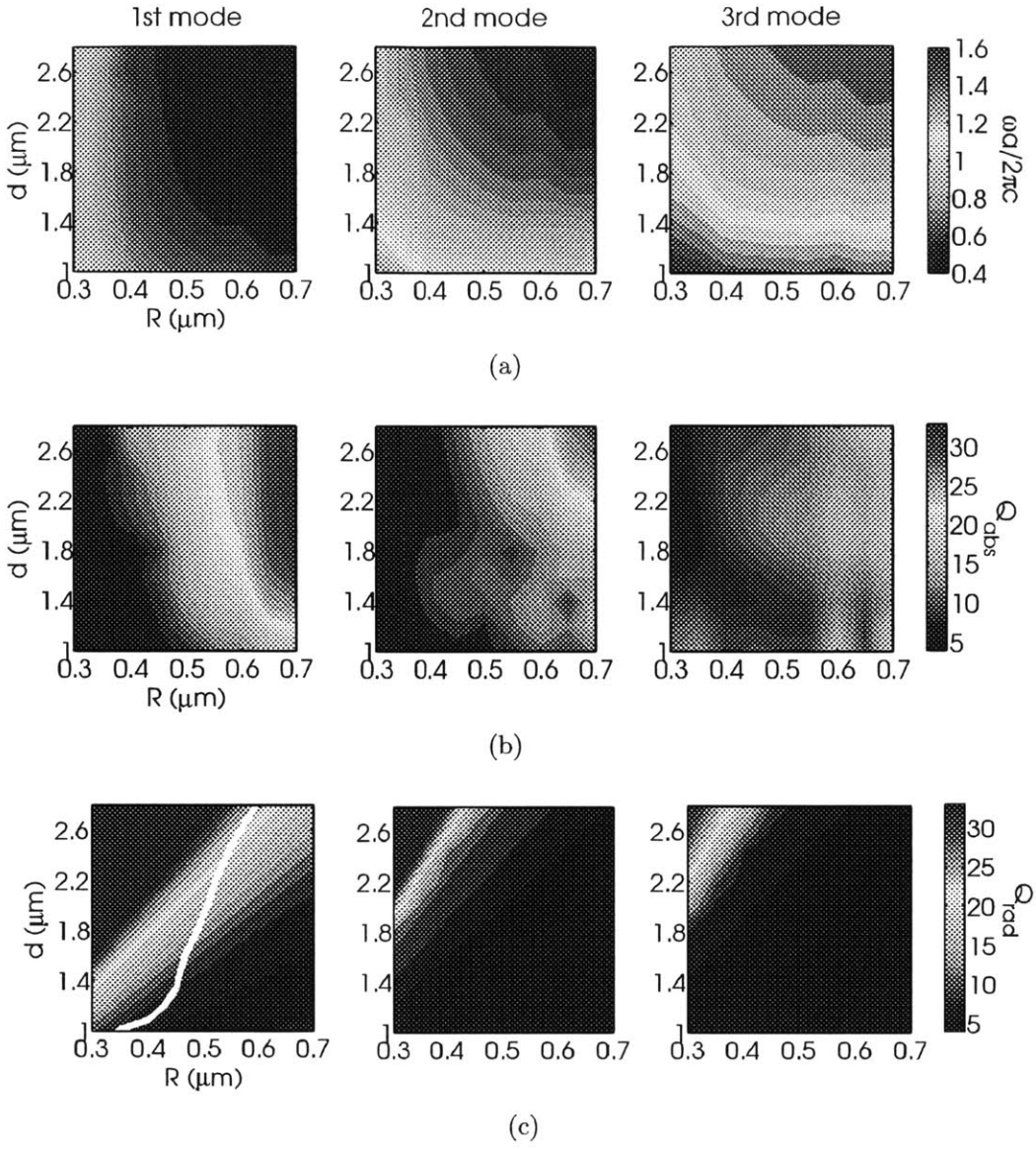

Figure 5-3: (a) Resonant mode frequency in units of $2\pi c/a$ with $a = 1$ μm, (b) Q_{abs}, and (c) Q_{rad} of the lowest three modes. The absorptive and radiative Q are plotted on the same color scale. Q-matching of the first resonance is indicated by the white line.

shown that

$$Q_{\text{rad}} \propto \left(\frac{d}{R}\right)^3 \tag{5.1}$$

through $Q_{\text{rad}} = \omega_o U / P_{\text{rad}}$. The stored field energy is approximately the product of the hole volume and the electric field intensity at the hole center, $U \approx \varepsilon_0 R^2 d |\mathbf{E}_{\text{center}}|^2$. The radiated power is the product of the Poynting field at the cavity opening and the area of the opening, $P_{\text{rad}} \approx R^2 |\mathbf{E}_{\text{opening}}|^2 / (c\mu_0)$. From simulations of holes with R and d varied separately one obtains $|\mathbf{E}_{\text{opening}}| / |\mathbf{E}_{\text{center}}| \approx 2R/d$, which gives $Q_{\text{rad}} \propto \omega_o d^3 / (cR^2)$. Expressing the resonant frequency ω_o in terms of the geometric parameters yields the desired result to leading order in d/R. Simulations confirm Eq. 5.1, but with an exponent slightly less than 3.

Q-matching is attained wherever the two surfaces, $Q_{\text{abs}}(R, d)$ and $Q_{\text{rad}}(R, d)$, intersect. For the first resonance this occurs on the white line in Fig. 5-3(c). Above the line Q_{rad} is too large, the hole is under-coupled to external radiation. Below it Q_{rad} is too small and the hole is over-coupled to external radiation, power can effectively couple into the hole, but it's trapped for too short a time to be absorbed. Critical coupling can be achieved by tuning the radius to increase Q_{rad} to a high enough value.

5.3 Effect of period

The optimal dimensions for an isolated hole may not be the same for a periodic array of holes, Q_{rad} may increase if the far field of neighboring holes interfere destructively. Moreover, Q-matching has been achieved for spherical waves converging onto the hole. The effect of a on Q_{rad} can be determined through a field-matching formalism

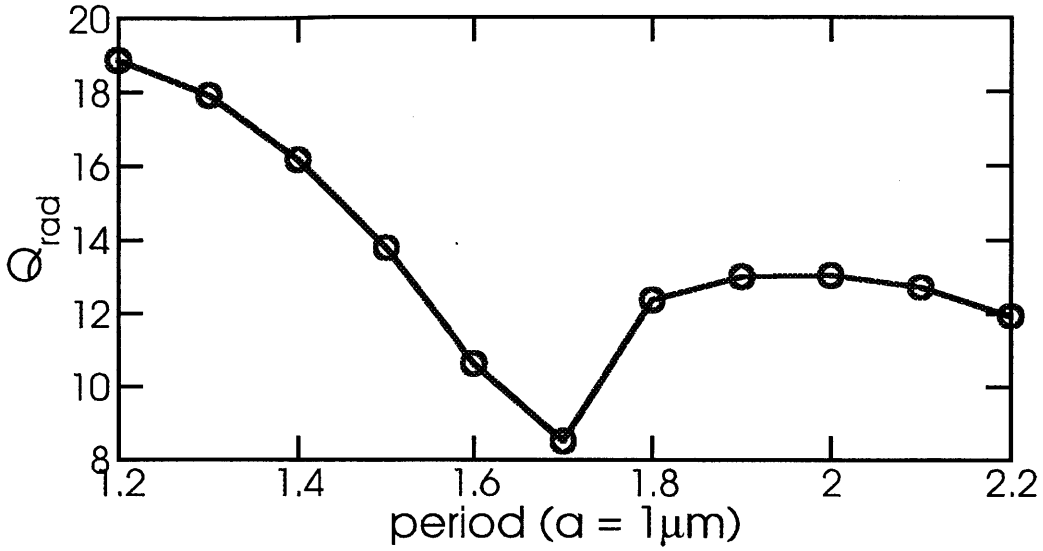

Figure 5-4: Q_{rad} versus period of unit cell with $R = 0.545\mu$m and $d = 1.89\mu$m. Resonance with a diffracted plane wave sets up an anti-crossing, visible as large jumps in Q_{rad}. Since we consider resonances that couple only to normal incidence, the period is bounded from above.

described in Ref. [125] where the field above the perfect conductor slab is expanded in a plane wave basis and the field inside the holes expanded as a linear combination of waveguide modes. The number of waveguide modes needed here is quite small, it is sufficient to use just the fundamental TE and TM waveguide modes since the cutoff frequencies of higher order modes lie far above the range of frequencies considered. From matching the parallel components of the fields, a scattering matrix connecting the waveguide amplitudes with the incident field is formed,

$$[G(\omega) - \epsilon(\omega)]\,\mathbf{E} = \mathbf{I} \tag{5.2}$$

where $\mathbf{E}$ is a two-component vector of the waveguide mode amplitudes, $\mathbf{I}$ is a two-component vector of the incident field overlap with each waveguide mode, $G(\omega)$ is a frequency dependent 2×2 matrix formed from the overlap of the waveguide modes and the plane waves above, and $\epsilon(\omega)$ is a diagonal matrix that determines the self-energy of the waveguide modes. By setting $\mathbf{I} = 0$, the poles of the scattering matrix can be found, giving both the resonant frequency and radiative rate. In addition the resonant field can be obtained; it is found that the near field is composed of diffracted, evanescent plane waves (i.e., those plane waves that carry no power away from the slab). Q_{rad} is typically larger than that of an isolated hole due to partial destructive interference of the far field. The period can change Q_{rad} by about 50% relative to the isolated hole Q_{rad} illustrated in Fig. 5-4 for the first resonance. Most of the variation in Q_{rad} occurs near periods where there exists diffracted plane waves that are resonant with a waveguide mode. During this resonance it is possible for Q_{rad} to be less than that of the isolated hole value. Q_{abs}, on the other hand, is not expected to change by more than a few percent for holes that are separated by a skin depth or more since that coupling is exponentially dependent on the separation [18]. Nonetheless, the Q-matching condition of the isolated holes can serve as a guide toward the optimal hole parameters for the photonic crystal slab.

Using the previously built intuition we simulate a tungsten photonic crystal with hole dimensions predicted to satisfy Q-matching, $R = 0.5\ \mu$m and $d = 1.89\ \mu$m, and period $a = 4.8\,\mu$m. A normally incident, linearly polarized plane wave is directed at the tungsten photonic crystal slab. Perfectly matched layers (PML) terminate the computational cell above the slab and periodic boundary condition ($\mathbf{k}_{\|} = 0$) on the sides. (PML is unnecessary below since the slab is opaque.) The absorptivity spectrum is calculated from the reflectivity spectrum, $A(\omega) = 1 - R(\omega)$. The emissivity spectrum, for normal emission, is obtained from the absorptivity spectrum

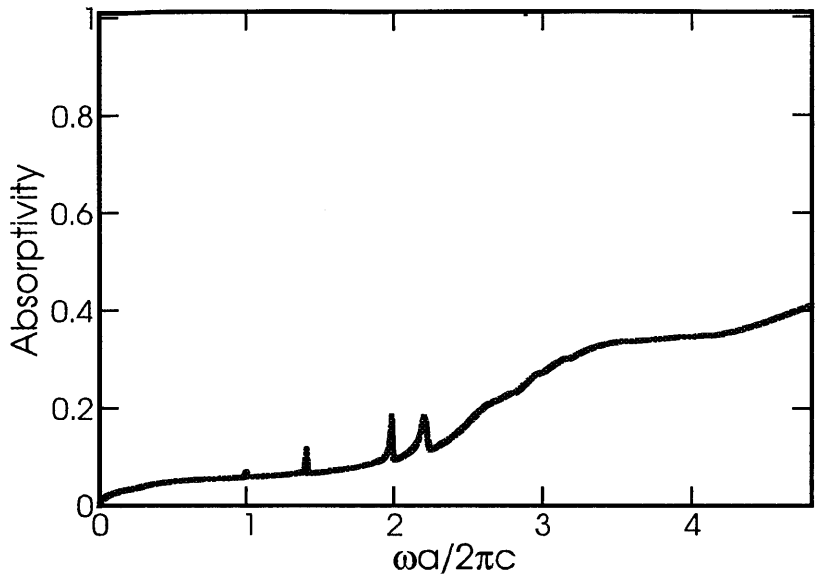

Figure 5-5: Absorption spectrum for the tungsten photonic crystal slab with $a = 4.8\,\mu$m, $R = 0.104a$, and $d = 0.394a$. Diffraction appears as sharp peaks and weak resonant peaks due to photonic crystal modes appear at approximately 2.7 and 3.4 $2\pi c/a$.

via Kirchhoff's law which states that for a body in thermal equilibrium, emissivity and absorptivity must match at each frequency, wave vector, and polarization [119, 126, 127]. Due to the large period, the emissivity spectrum of the $a = 4.8\,\mu$m crystal, Fig. 5-5, is essentially that of flat tungsten with sharp diffraction peaks and broadened photonic crystal resonances superimposed. The holes occupy a small fraction of the surface, and the photonic crystal resonances radiate into many allowed diffracted plane waves increasing the reflectivity. The period does not seriously spoil Q-matching; Q_{rad} of the first resonance for the isolated hole and photonic crystal slab are 14.3 and 12.7, respectively. To realize a stronger frequency selectivity it is

necessary to adjust a; plotted in Fig. 5-6 are the emissivity spectra for various a. As a is decreased, the first resonant peak eventually appears below the diffraction limit, $\omega a/2\pi c = 1$. Further reduction of a pushes the diffraction limit above additional resonances, increasing the bandwidth of the high emissivity region. This can be continued up to $a = 2R$ at which point the hole resonances are strongly coupled to each other through the tungsten side walls in addition to the nonradiative coupling via evanescent plane waves. If the period is further reduced ($a < 2R$) creating an array of posts on the surface, then the photonic crystal resonances can no longer be described as coupled waveguide resonances, such as for $a = 0.75\,\mu$m where tungsten posts occupy 7% of the surface. Note that at wavelengths much larger than a, different absorptivities occur due to the varying ratios of air hole to tungsten side wall volumes. In the long wavelength limit the free electron density makes the dominant contribution to the permittivity and effective medium theory is valid. Decreasing the tungsten fraction decreases the free electron density. This lowers the effective plasma frequency which increases the absorption rate.

5.4 Coupled-mode theory

With a handle on the resonant frequency and both the absorptive and radiative rates, we now focus on the $a = 1.2\,\mu$m emissivity spectrum and understand it through temporal coupled-mode theory [128, 129, 130]. The tungsten photonic crystal slab can be thought of as a multimode resonator, illustrated in Fig. 5-7. Associated with each resonance is a resonant frequency ω_i, absorptive lifetime $\tau_{\text{abs},i}$, and radiative lifetime $\tau_{\text{rad},i}$. In addition they can radiatively couple to each other with a lifetime τ_{ij} $(i \neq j)$ on the order of $\tau_{\text{rad},i}$ [131]. The coupled-mode equations for the multimode

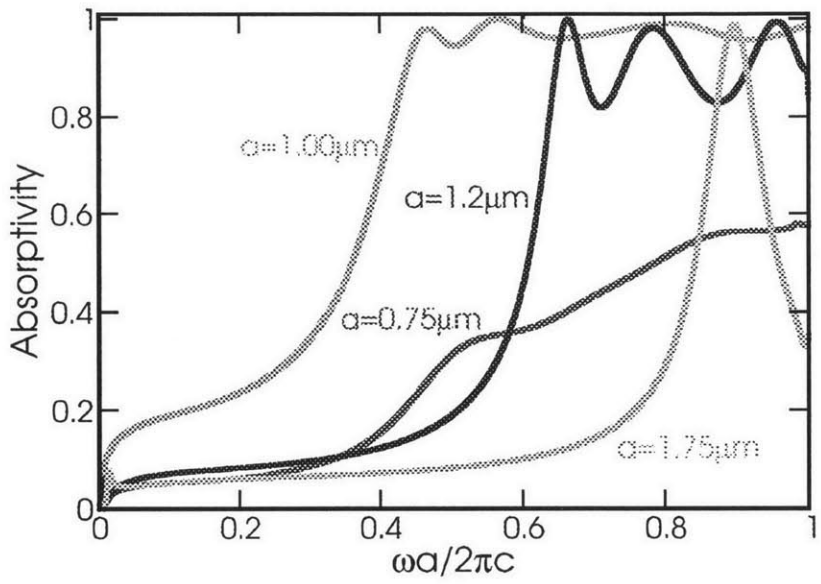

Figure 5-6: Absorption spectra for photonic crystal slabs with various a but R and d fixed at 0.5 and 1.89 μm, respectively.

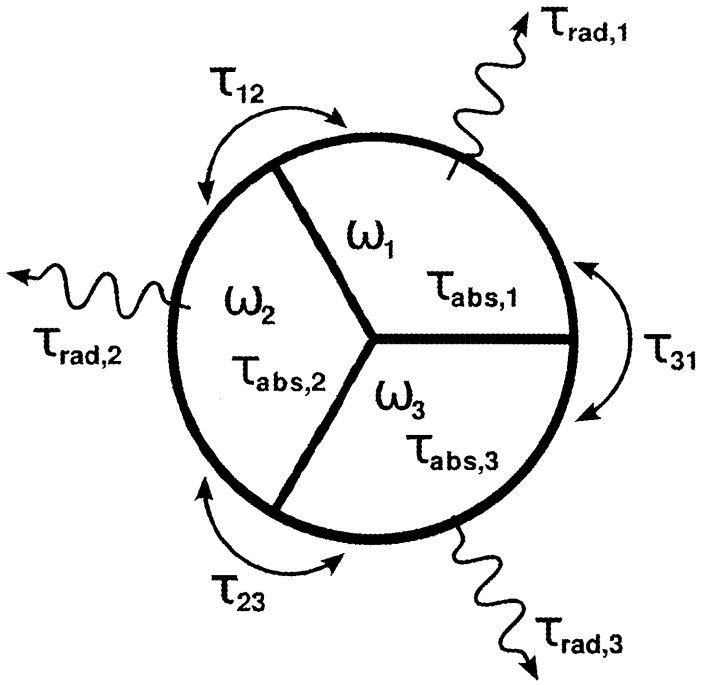

Figure 5-7: A multimode resonator with resonant frequencies ω_i, absorptive and radiative lifetimes $\tau_{\text{abs},i}$ and $\tau_{\text{rad},i}$, respectively. Resonances i and j radiatively couple to each other with rate $1/\tau_{ij}$.

resonator are,

$$\frac{d\mathbf{a}}{dt} = (-i\Omega_0 - \Gamma)\mathbf{a} + D^T s_+ \tag{5.3}$$

$$s_- = Cs_+ + D\mathbf{a}, \tag{5.4}$$

from which the reflectivity is $R = |s_-/s_+|^2$. The three component vector $\mathbf{a}$ describes the resonant mode amplitudes, Ω_0 is a 3×3 diagonal matrix of the resonant mode frequencies, Γ is a 3×3 matrix of decay rates, D is 1×3 matrix of the resonance-port coupling amplitudes, C is the direct pathway scattering matrix/amplitude, and $s_\pm$ are the incoming/outgoing port amplitudes. The decay rate matrix Γ can be

separated into a radiative contribution Γ_r and an absorptive contribution Γ_a with $\Gamma_{r,ii} = 1/\tau_{\text{rad},i}$ and $\Gamma_{a,ii} = 1/\tau_{\text{abs},i}$. The resonance-resonance coupling rates, $1/\tau_{ij}$, are given by the off-diagonal elements of Γ_r and are dependent on $\Gamma_{r,ii}$. The dependence comes about through the matrix relation $2\Gamma_r = D^\dagger D$, which is a consequence of energy conservation and reciprocity. In addition, the direct pathway scattering matrix constrains the phases of D via the relation $CD^* = -D$. Since the front surface absorption is neglected, the front surface is approximated as a perfect conductor and C is set to -1. The phase of the elements of D depend on how many ways the photonic crystal resonances can couple to each other [131]. In the case of hole depth equal to slab thickness, the photonic crystal resonances couple via the top and bottom, and if the phases of the resonances are different at either opening, as in the case of resonances with opposite parity, then the resonances will not couple, i.e., $\tau_{ij} \to \infty$. Here the hole depth is less than the slab thickness by more than a couple skin depths, parity is broken, and so all resonances will radiatively couple to one another. This also implies that the resonance-port coupling amplitudes will have the same phase.

From FDTD simulations we obtain ω_i, $\tau_{\text{abs},i}$, and $\tau_{\text{rad},i}$ for the first three resonances. In particular, $\tau_{\text{rad},i}$ is obtained from simulating a unit cell of the photonic crystal with the radius widened by a skin depth. The resulting emissivity spectrum is compared with the emissivity spectrum obtained from the full FDTD simulation in Fig. 5-8. Since coupled-mode theory is a perturbation theory, it is most accurate for resonances with total $Q \gg 1$; here the resonances have total Q of 8.0, 4.4, and 6.3, respectively, and unsurprisingly, the spectra display some differences. The resonances above the diffraction limit of $\omega = 2\pi c/a$ are not taken into account, doing so requires not only their resonant frequencies and lifetimes, but also modifying the couple-mode equations to include the extra ports that correspond to diffracted plane waves. Clearly this would greatly complicate the coupled-mode equations– account-

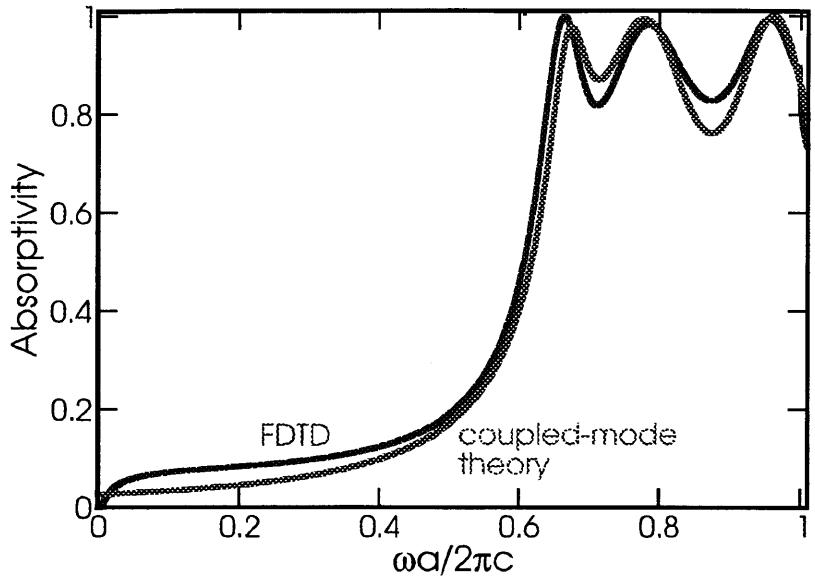

Figure 5-8: Absorptivity spectrum for $a = 1.2\,\mu$m calculated by FDTD simulation (blue) and coupled-mode theory (red).

ing for just the first order diffraction would require $s_{\pm}$ to be a 5×1 vector, D a 5×3 matrix, and C a 5×5 frequency-dependent matrix. It is also clear that the coupled-mode equations here will not work for frequencies much less than the cut-off frequency where the absorption is due primarily to the front surface of tungsten. In principle it can be accounted for in the coupled-mode equations by considering the front surface absorption as another port [131]. Surface plasmons due to tungsten's permittivity can be ignored; while there are material resonances below $\omega a/2\pi c = 1$, the loss rates associated with the surface plasmons are too large to allow significant absorption peaks.

5.5 Applications and conclusions

Demonstrating that it is possible to predict the emissivity spectra with only a few input parameters– the optical constants of tungsten, a, R, and d– attention can be directed toward applications. In TPV and solar TPV (STPV), the radiated photons from a high temperature radiator are captured and converted into electron-hole pairs via a photovoltaic cell [120, 121]. In the case of STPV, concentrated sunlight is used to heat the tandem absorber-emitter structure which then radiates onto a photovoltaic cell [132, 133]. In both cases, the emitter is heated to over 1000 K. The selective emitter described here can dramatically improve both the efficiency and power density of the TPV/STPV system by enhancing the above bandgap energy photons that directly generate electron-hole pairs in the PV cell, and suppressing low-energy photons that would only heat the photovoltaic cell. Moreover retaining the low-energy photons contribute toward keeping the emitter hot [134]. One possible structure would be the tungsten photonic crystal in Fig. 5-8 which has a cutoff frequency of $0.67\,\mathrm{eV}/\hbar$. It can be made to match the $0.6\,\mathrm{eV}/\hbar$ bandgap of InGaAs [122] by slightly widening the holes.

Another potential application of the selective emitters is higher efficiency tungsten incandescent elements. The tungsten filament is notoriously inefficient, less than 5% of the energy radiated is in the visible spectrum, due to the fact that the temperature of the filament, about 2800 K, implies via Wien's law a peak emitted wavelength slightly over 1 μm and that tungsten displays significant absorption in the near-IR and not enough absorption in the visible. Previous work has considered the use of a separate 2D metallic photonic crystal to act as a low-pass filter [134], those photons with wavelengths greater than the cutoff of the filter are reflected back to the hot filament. However, separating the filter and filament function lead

to added complexity with alignment and thermal separation. Patterning a photonic crystal on the surface of tungsten can address the issue of low visible radiation emission. A nonlinear optimization package [103] is used to find the neighborhood of the optimal photonic crystal parameters and the extent of improvement. The product of luminous flux and luminous efficiency serves as the figure of merit to optimize. The luminous flux is defined as the amount of useful radiation, i.e., the product of the emissivity spectrum, blackbody spectrum, and the eye's luminosity function which describes the eye's visual sensitivity to different wavelengths. It is approximately a gaussian centered at 0.55μm with a FWHM of 0.1μm [135]. Luminous efficiency is defined as the ratio of luminous flux to total radiated flux. The emissivity spectrum is calculated via the coupled-mode theory outlined above with semi-analytical expressions for all coupled-mode parameters. It is found that the optimal a, R, and d are 0.46μm, 0.15μm, and 0.35μm, respectively. The luminous flux is double that of flat tungsten, and the luminous efficiency is 34% larger than flat tungsten's. Plotting the emissivity spectrum shows that the peak is placed just above 0.55μm. The single resonance possesses a total Q of 2.55; clearly the conditions for coupled-mode theory are violated and FDTD simulations are needed to truly find the optimal set of parameters. For the same parameters FDTD simulations predict an improvement of 92% for the luminous flux and 30% for the luminous efficiency. In each case the relative difference from the semi-analytic prediction is less than 10%. While the photonic crystal improves the performance of the tungsten incandescent element, compared to current alternatives on the market, fluorescent and LED bulbs, the gains are not nearly enough. However this does not rule out the possibility of using other kinds of resonances such as surface plasmons.

In conclusion we have demonstrated how Q-matching, via the geometrical parameters, can be used to tailor the emissivity spectrum of 2D metallic photonic crystals.

Because the thermal radiation field is incoherent, the emissivity at all $\mathbf{k}_{\|}$ is needed. Since the resonant peaks are due to photonic crystal resonances arising from coupled hole resonances, it is expected that the location and shape of the resonant peaks change little with $\mathbf{k}_{\|}$ [18]. Therefore the emissivity spectrum, at least the portion below the onset of diffraction, should change little and continue to display high selectivity. Finally a fabricated photonic crystal is expected to have some disorder. While moderate disorder in the hole radius and depth will mainly red-shift and broaden the resonance peaks through a spread in the resonant frequencies, the same amount of disorder in the period is expected to be more destructive.

Chapter 6

Conclusion

In this thesis I've explored a wide range of phenomena in photonics: self-assembly (Chapter 2), zero-group velocity modes (Chapter 3), and tailored absorption and emission spectra (Chapters 4 & 5). A few more comments can be said about each. While self-assembly and colloidal photonic crystals can provide a simpler route toward fabricating 3D photonic crystals, issues related to the use of complex building blocks must be addressed. The first issue is the separation of the tetrahedra from spheres, dimers, and trimers that are also produced during the nucleation and conglomeration stage. This is still a challenge. The other issue is that of orienting the tetrastacks properly; this could be circumvented by using external fields and coating the tetrastacks to ensure that they stack properly. Another possible solution would be to envelop the tetrahedra with a spherical sacrificial coating. These spheres are then used to build the crystal. Once this is done the sacrificial coating can be etched away.

In Chapter 3, anomalous regions in two-dimensional band structures have been identified. The modes in these regions have an effective wavevector that makes an

obtuse angle with the group velocity.

In Chapter 4, we have found that sizable gains can be realized: over 40% relative to uncoated cells and almost 4% relative improvement going from 1 to 2 front coatings. Moreover for 1D coatings, the majority of the benefit is realized with just the first few layers. However, the simplicity of 1D front coatings is also their weakness; performance is limited by weak absorption in the long wavelength part of the solar spectrum. An area of future research is the use of back-surface correlated texturing. By optimizing over a spread of periods it may be possible to couple into guided modes in the near-IR and attain larger improvements in the short circuit current. Of course the front coatings must be optimized simultaneously with the back texturing to account for increased absorption in the longer wavelengths.

There is also more to be done with the 2D selective emitter described in Chapter 5. While focus has been on circular holes, it is clear that this approach will work with any type of holes. In fact, selective emissivity may benefit from less symmetric cross-sections. For example, elliptical holes break rotational symmetry and lift the degeneracy between the counter-rotating modes effectively doubling the number of peaks that appear below the diffraction limit. Another area of future work would be to explore the benefit of quasi-crystalline order. It is known that extraordinary transmission, which relies on resonant photonic crystal modes, can be observed on a thin film that has only orientational order [136, 137]. It is reasonable to expect the appearance of photonic quasicrystal modes here as well. Again, the idea would be to broaden the high emissivity range with more resonances.

Bibliography

[1] C.M. Herzinger, B. Johs, W.A. McGahan, J.A. Woollam, and W. Paulson. Ellipsometric determination of optical constants for silicon and thermally grown silicon dioxide via a multi-sample, multi-wavelength, multi-angle investigation. *J. Appl. Phys.*, 83:3323–3336, 1998.

[2] William H. Press, Saul A. Teukolsky, William T. Vetterling, and Brian P. Flannery. *Numerical Recipes, The Art of Scientific Computing.* Cambridge University Press, New York, 2007.

[3] E. Yablonovitch. Inhibited spontaneous emission in solid-state physics and electronics. *Phys. Rev. Lett.*, 58:2059–2062, 1987.

[4] Sajeev John. Strong localization of photons in certain disordered dielectric superlattices. *Phys. Rev. Lett.*, 58:2486–2489, 1987.

[5] J. D. Joannopoulos, S. G. Johnson, J. N. Winn, and R. D. Meade. *Photonic Crystals: Molding the Flow of Light.* Princeton Univ. Press, second edition, 2008.

[6] R. A. Shelby, D. R. Smith, and S. Schultz. Experimental verification of a negative index of refraction. *Science*, 292(5514):77–79, 2001.

[7] Chiyan Luo, Steven G. Johnson, J. D. Joannopoulos, and J. B. Pendry. All-angle negative refraction without negative effective index. *Phys. Rev. B*, 65:201104, 2002.

[8] J. B. Pendry, D. Schurig, and D. R. Smith. Controlling electromagnetic fields. *Science*, 312(5781):1780–1782, 2006.

[9] Ulf Leonhardt. Optical conformal mapping. *Science*, 314(5781):1777–1780, 2006.

[10] D. Schurig, J. J. Mock, B. J. Justice, S. A. Cummer, J. B. Pendry, A. F. Starr, and D. R. Smith. Metalmaterial electromagnetic cloak at microwave frequencies. *Science*, 314(5801):977–980, 2006.

[11] Shanhui Fan, Pierre R. Villeneuve, J. D. Joannopoulos, and H. A. Haus. Channel drop tunneling through localized states. *Phys. Rev. Lett.*, 80(5):960–963, 1998.

[12] Pete Vukusic and Ian Hooper. Directionally controlled fluorescence emission in butterflies. *Science*, 310(5751):1151, 2005.

[13] Pete Vukusic and J. Roy Sambles. Photonic structures in biology. *Nature*, 424(6950):852–855, 2003.

[14] Jeremy W. Galusha, Lauren R. Richey, John S. Gardner, Jennifer N. Cha, and Michael H. Bartl. Discovery of a diamond-based photonic crystal structure in beetle scales. *Phys. Rev. E*, 77(5):050904, 2008.

[15] Andrew R. Parker, Ross C. McPhedran, David R. McKenzie, Lindsay C. Botten, and Nicolae-Alexandru P. Nicorovici. Aphrodite's irridescence. *Nature*, 409:36–37, 2001.

[16] N. W. Ashcroft and N. D. Mermin. *Solid State Physics.* Thompson Learning, Inc., first edition, 1976.

[17] S. L. McCall, P. M. Platzman, R. Dalichaouch, David Smith, and S. Schultz. Microwave propagation in two-dimensional dielectric lattices. *Phys. Rev. Lett.*, 67(15):2017–2020, 1991.

[18] Amnom Yariv, Yong Xu, Reginald K. Lee, and Axel Scherer. Coupled-resonator optical waveguide: a proposal and analysis. *Opt. Lett.*, 24:711–713, 1999.

[19] Youg Xu, Reginald K. Lee, and Amnon Yariv. Propagation and second-harmonic generation of electromagnetic waves in a coupled-resonator optical waveguide. *J. Opt. Soc. Am. B*, 17(3):387–400, 2000.

[20] M. Povinelli, Steven Johnson, and J. Joannopoulos. Slow-light, band-edge waveguides for tunable time delays. *Opt. Express*, 13(18):7145–7159, 2005.

[21] Joshua N. Winn, Yoel Fink, Shanhui Fan, and J. D. Joannopoulos. Omnidirectional reflection from a one-dimensional photonic crystal. *Opt. Lett.*, 23(20):1573–1575, 1998.

[22] Yoel Fink, Joshua N. Winn, Shanhui Fan, Chiping Chen, Jurgen Michel, John D. Joannopoulos, and Edwin L. Thomas. A dielectric omnidirectional reflector. *Science*, 282(5394):1679–1682, 1998.

[23] Hideo Kosaka, Takayuki Kawashima, Akihisa Tomita, Masaya Notomi, Toshiaki Tamamura, Takashi Sato, and Shojiro Kawakami. Self-collimating phenomena in photonic crystals. *Appl. Phys. Lett.*, 74(9):1212–1214, 1999.

[24] Masaru Onoda and Tetsuyuki Ochiai. Designing spinning bloch states in 2d photonic crystals for stirring nanoparticles. *Phys. Rev. Lett.*, 103(3):033903, 2009.

[25] T. T. Ngo, C. M. Liddell, M. Ghebrebrhan, and J. D. Joannopoulos. Tetrastack: Colloidal diamond-inspired structure with omnidirectional photonic band gap for low refractive index contrast. *Applied Physics Letters*, 88(24):241920, 2006.

[26] M. Ghebrebrhan, M. Ibanescu, S.G. Johnson, M. Soljacic, and J.D. Joannopoulos. Distinguishing zero-group-velocity modes in photonic crystals. *Phys. Rev. A*, 76(6):063810, 2007.

[27] Michael Ghebrebrhan, Peter Bermel, Yehuda Avniel, John D. Joannopoulos, and Steven G. Johnson. Global optimization of silicon photovoltaic cell front coatings. *Opt. Express*, 17(9):7505–7518, 2009.

[28] M. Ghebrebrhan, P. Bermel, Y. X. Yeng, I. Celanovic, M. Soljacic, and J.D. Joannopoulos. *in submission.*

[29] R.A. Shelby, D.R. Smith, and S. Schultz. Experimental verification of a negative index of refraction. *Science*, 292(77):5514, 2001.

[30] Victor G. Veselago. The electrodynamics of substances with simultaneously negative values of ε and μ. *Sov. Phys. Uspekhi*, 10:509–514, 1968.

[31] J. B. Pendry. Negative refraction makes a perfect lens. *Phys. Rev. Lett.*, 85(18):3966–3969, 2000.

[32] J. Zhao, A. Wang, M.A. Green, and F. Ferrazza. Novel 19.8% efficient 'honeycomb' textured multicrystalline and 24.4% monocrystalline silicon solar cells. *Appl. Phys. Lett.*, 73:1991–1993, 1998.

[33] William Shockley and Hans J. Queisser. Detailed balance limit of efficiency of p-n junction solar cells. *J. Appl. Phys.*, 32:510, 1961.

[34] S. Noda, K. Tomoda, N. Yamamoto, and A. Chutinan. Full three-dimensional photonic bandgap crystals at near-infrared wavelengths. *Science*, 289(5479):604–606, 2000.

[35] Jordi Martorell and N. M. Lawandy. Observation of inhibited spontaneous emission in a periodic dielectric structure. *Phys. Rev. Lett.*, 65(15):1877–1880, 1990.

[36] Hideki Hirayama, Tetsuko Hamano, and Yoshinobu Aoyagi. Novel surface emitting laser diode using photonic band-gap crystal cavity. *Applied Physics Letters*, 69(6):791–793, 1996.

[37] H. Han, S. Vijayalakshmi, A. Lan, Z. Iqbal, H. Grebel, E. Lalanne, and A. M. Johnson. Linear and nonlinear optical properties of single-walled carbon nanotubes within an ordered array of nanosized silica spheres. *Applied Physics Letters*, 82(9):1458–1460, 2003.

[38] S.Y. Lin, J.G. Fleming, D. L. Hetherington, B.K. Smith, R. Biswas ans K.M. Ho, M.M. Sigalas, W. Zubrzycki, S.R. Kurtz, and Jim Bur. A three-dimensional photonic crystal operating at infrared wavelengths. *Nature*, 394:251–253, 1998.

[39] Minghao Qi, Elefterios Lidorikis, Peter T. Rakich, Steven G. Johnson, J.D. Joannopoulos, Erich P. Ippen, and Henry I. Smith. A three-dimensional optical photonic crystal with designed point defects. *Nature*, 429:538–542, 2004.

[40] Peigen Ni, Bingying Cheng, and Daozhong Zhang. Inverse opal with an ultraviolet photonic gap. *Appl. Phys. Lett.*, 80(11):1879–1881, 2002.

[41] Kurt Busch and Sajeev John. Photonic band gap formation in certain self-organizing systems. *PRE*, 58(3):3896–3908, 1998.

[42] H. S. Sözüer, J. W. Haus, and R. Inguva. Photonic bands: Convergence problems with the plane-wave method. *Phys. Rev. B*, 45(24):13962–13972, 1992.

[43] K. M. Ho, C. T. Chan, and C. M. Soukoulis. Existence of a photonic gap in periodic dielectric structures. *Phys. Rev. Lett.*, 65(25):3152–3155, 1990.

[44] F. Garcia-Santamaria, H.T. Miyazaki, A. Urquia, M. Ibisate, M. Belamonte, N. Shinya, F. Meseguer, and C. Lopez. Nanorobotic manipulation of microspheres for on-chip diamond architectures. *Advanced Materials*, 14(16):1144–1147, 2002.

[45] Younan Xia, Byron Gates, and Yadong Yin. Current chemistry: Building complex structures from monodisperse spherical colloids. *Australian Journal of Chemistry*, 54(5):287–290, 2001.

[46] Steven G. Johnson and J. D. Joannopoulos. Block-iterative frequency-domain methods for Maxwell's equations in a planewave basis. *Opt. Express*, 8(3):173–190, 2001.

[47] C. Lopez. Materials aspects of photonic crystals. *Advanced Materials*, 15(50):1679–1704, 2003.

[48] Zhi-Yuan Li, Jian Wang, and Ben-Yuan Gu. Full band gap in fcc and bcc photonic band gaps structure: Non–spherical atom. *Journal of the Physical Society of Japan*, 67(9):3288–3291, 1998.

[49] Vinothan N. Manoharan, Mark T. Elsesser, and David J. Pine. Dense packing and symmetry in small clusters of microspheres. *Science*, 301(5632):483–487, 2003.

[50] Y. Yin and Y. Xia. Self-assembly of monodispersed spherical colloids into complex aggregates with well-defined sizes, shapes, and structures. *Advanced Materials*, 13(4):267–271, 2001.

[51] I. Lee, H. Zheng, M.F. Rubner, and P.T. Hammond. Controlled cluster size in patterned particle arrays via directed adsorption on confined surfaces. *Advanced Materials*, 14(8):572–577, 2002.

[52] *Polysciences Inc. Catalog 146*, 2002-2003.

[53] C.M. Liddell and C.J. Summers. Monodispersed zns dimers, trimers, and tetramers for lower symmetry photonic crystal lattices. *Advanced Materials*, 15(20):1715–1719, 2003.

[54] C. M. Liddell and C. J. Summers. Nonspherical zns colloidal building blocks for three-dimensional photonic crystals. *Journal of Colloid and Interface Science*, 274(1):103 – 106, 2004.

[55] Y. Lu, Y. Yin, and Y. Xia. Three-dimensional photonic crystals with non-spherical colloids as building blocks. *Advanced Materials*, 13(6):415–420, 2001.

[56] Pochi Yeh. *Optical Waves in Layered Media.* Wiley, New York, 1988.

[57] J. E. Sipe. Vector $\mathbf{k} \cdot \mathbf{p}$ approach for photonic band structures. *Phys. Rev. E*, 62:5672–5677, 2000.

[58] M. Notomi. Theory of light propagation in strongly modulated photonic crystals: Refractionlike behavior in the vicinity of the photonic band gap. *Phys. Rev. B*, 62:10696–10705, 2000.

[59] Mihai Ibanescu, Steven G. Johnson, David Roundy, Chiyan Luo, Yoel Fink, and John D. Joannopoulos. Anomalous dispersion relations by symmetry breaking in axially uniform waveguides. *Phys. Rev. Lett.*, 92:063903, 2004.

[60] Mihai Ibanescu, Steven G. Johnson, David Roundy, Yoel Fink, and John D. Joannopoulos. Microcavity confinement based on anomalous zero group-velociy waveguide mode. *Opt. Lett.*, 30:552–554, 2005.

[61] V. A. Mandelshtam and H. S. Taylor. Harmonic inversion of time signals and its applications. *J. Chem. Phys.*, 107(17):6756–6769, 1997.

[62] Allen Taflove and Susan C. Hagness. *Computational Electrodynamics: The Finite-Difference Time-Domain Method.* Artech, Norwood, MA, 2000.

[63] A. Farjadpour, David Roundy, Alejandro Rodriguez, M. Ibanescu, Peter Bermel, J. D. Joannopoulos, Steven G. Johnson, and G. W. Burr. Improving accuracy by subpixel smoothing in the finite-difference time domain. *Opt. Lett.*, 31:2972–2974, 2006.

[64] Miguel A. Contreras, Brian Egaas, K. Ramanathan, J. Hiltner, A. Swartzlander, F. Hasoon, and Rommel Noufi. Progress toward 20% efficiency in cu(in,ga)se2 polycrystalline thin-film solar cells. *Prog. Photovolt: Res. Appl.*, 7:311–316, 1999.

[65] G.S. Was, V. Rotberg, D. Platts, and J. Bomback. Optical properties of ti and n implanted soda lime glass. *Appl. Phys. Lett.*, 66:142–144, 1995.

[66] S. Chaudhuri, D. Bhattacharyya, A.B. Maity, and A.K. Pal. Surface coatings for solar application. *Mat. Sci. Forum*, 246:181–206, 1997.

[67] C.M. Lampert. International development and advances in solar selective absorbers. *Proc. SPIE*, 3138:134–145, 1997.

[68] A. Chandra and M. Mishra. Solar absorption behavior of multilayer stacks. *Energ. Convers. Manage.*, 25:387–390, 1985.

[69] O. Abreu and G. Best. Transmission, reflexion and absorption of visible radiation by the multiple covers of flat plate solar collectors. *Sol. Energ. Mater.*, 3:371–380, 1980.

[70] L. DeSandre, D.Y. Song, H.A. MacLeod, M.R. Jacobson, and D.E. Osborn. Thin-film multilayer filter designs for hybrid solar energy conversion systems. *Proc. SPIE*, 562:155–159, 1985.

[71] J.H. Schoen and E. Bucher. Computer modeling of the performance of some metal/dielectric multilayers for high-temperature solar selective absorbers. *Sol. Energ. Mater. Sol. C.*, 43:59–65, 1996.

[72] M. Farooq and M.G. Hutchins. A novel design in composites of various materials for solar selective coatings. *Sol. Energ. Mater. Sol. C.*, 71:523–535, 2002.

[73] J. Sukmanowski, C. Paulick, O. Sohr, K. Andert, and F.X. Royer. Light absorption enhancement in thin silicon layers. *J. Appl. Phys.*, 88:2484–2489, 2000.

[74] J.J. Hanak, V. Korsun, and J.P. Pellicane. Optimization studies of materials in hydrogenated amorphous silicon solar cells. Number 2nd in E.C. Photovoltaic Sol. Energ. Conf., pages 270–277, 1979.

[75] M. Kuo, D. J. Poxson, Y. S. Kim, F. W. Mont, J. K. Kim, E. F. Schubert, and S. Lin. Realization of a near-perfect antireflection coating for silicon solar energy utilization. *Opt. Lett.*, 33:2527–2529, 2008.

[76] ASTMG173-03. *Standard Tables for Reference Solar Spectral Irradiances: Direct Normal and Hemispherical on 37 degree Tilted Surface.* ASTM International, West Conshohocken, Pennsylvania, 2005.

[77] P. Nubile. Analytical design of antireflection coatings for silicon photovoltaic devices. *Thin Solid Films*, 342:257–261, 1999.

[78] J. Zhao and M.A. Green. Optimized antireflection coatings for high-efficiency silicon solar cells. *IEEE Trans. Electron Dev.*, 38:1925, 1991.

[79] F. Zhu, P. Jennings, J. Cornish, G. Hefter, and K. Luczak. Optimal optical design of thin-film photovoltaic devices. *Sol. Energ. Mat. Sol. C.*, 49:163–169, 1997.

[80] M. Cid, N. Stem, C. Brunetti, A.F. Beloto, and C.A.S. Ramos. Improvements in anti-reflection coatings for high-efficiency silicon solar cells. *Surface and Coatings Tech.*, 106:117–120, 1998.

[81] Henning Nagel, Armin G. Aberle, and Rudolf Hezel. Optimised antireflection coatings for planar silicon solar cells using remote pecvd silicon nitride and porous silicon dioxide. *Prog. Photovoltaics: Res. Appl.*, 7:245–260, 1999.

[82] B.S. Thornton and Q.M. Tran. Optimum design of wideband selective absorbers with provision for specified included layers. *Sol. Energy*, 20:371–377, 1978.

[83] C.K. Carniglia and J.H. Apfel. Maximum reflectance of multilayer dielectric mirrors in the presence of slight absorption. *J. Opt. Soc. Am.*, 70:523–534, 1980.

[84] D.R. Gibson and P.H. Lissberger. Use of the concept of equivalent layers in the design of multilayer dielectric reflectors with minimum absorption. *Optica Acta*, 27:1295–1299, 1980.

[85] Rolf Brendel. *Thin-Film Crystalline Silicon Solar Cells.* Wiley-VCH, Weinheim, Germany, 2003.

[86] B.S. Richards. Single-material tio2 double-layer antireflection coatings. *Sol. Energy Mat. Sol. C.*, 79:369–390, 2003.

[87] A. Mahdjoub and L. Zighed. New designs for graded refractive index antireflection coatings. *Thin Solid Films*, 478:299–304, 2005.

[88] Jianhua Zhao, Aihua Wang, Patrick Campbell, and Martin A. Green. A 19.8% efficient honeycomb multicrystalline silicon solar cell with improved light trapping. *IEEE Trans. Electron Dev.*, 46:1978–1983, 1999.

[89] M. Lipinski, P. Zieba, S. Kluska, M. Sokolowski, and H. Czternastek. Optimization of sinx:h layer for multicrystalline silicon solar cells. *Opto-Electron. Rev.*, 12:41–44, 2004.

[90] Mukul Agrawal and Peter Peumans. Broadband optical absorption enhancement through coherent light trapping in thin-film photovoltaic cells. *Opt. Express*, 16:5385–5396, 2008.

[91] Lifeng Li. Formulation and comparison of two recursive matrix algorithms for modeling layered diffraction gratings. *J. Opt. Soc. Am. A*, 13:1024–1035, 1996.

[92] D.M. Whittaker and I.S. Culshaw. Scattering-matrix treatment of patterned multilayer photonic structures. *Phys. Rev. B*, 60:2610–2618, 1999.

[93] K. S. Yee. Numerical solution of inital boundary value problems involving maxwell's equations in isotropic media. *IEEE Trans. Attennas Propag.*, AP-14:302–307, 1966.

[94] J.P. Berenger. A perfectly matched layer for the absorption of electromagnetic waves. *J. Comp. Phys.*, 114:185–200, 1994.

[95] Peter Bermel, Chiyan Luo, Lirong Zeng, Lionel Kimerling, and John D. Joannopoulos. Improving thin-film crystalline silicon solar cell efficiencies with photonic crystals. *Opt. Express*, 15:16986–17000, 2007.

[96] A. H. G. Rinnooy Kan and G. T. Timmer. Stochastic global optimization methods. *Math. Program.*, 39:27–78, 1987.

[97] J. Nocedal. Updating quasi-newton matrices with limited storage. *Math. Comput.*, 35:773–782, 1980.

[98] Ladislav Luksan. Plis.for. Limited-memory BFGS method based on vector recurrences for large-scale unconstrained and box constrained minimization.

[99] Sergei Kucherenko and Yury Sytsko. Application of deterministic low-discrepancy sequences in global optimization. *Computational Optimization and Applications*, 30:297–318, 2005.

[100] P. Bratley and B. L. Fox. Algorithm 659: Implementing sobol's quasirandom sequence generator. *ACM Trans. Math. Soft.*, 14:88–100, 1988.

[101] S. Joe and F. Y. Kuo. Remark on algorithm 659: Implementing sobol's quasirandom sequence generator. *ACM Trans. Math. Soft.*, 29:49–57, 2003.

[102] J. M. Gablonsky and C. T. Kelley. A locally-biased form of the direct algorithm. *J. Global Optim.*, 21(1):27–37, 2001.

[103] Steven G. Johnson.

[104] G. Strang. *Computational Science and Engineering.* Wellesley-Cambridge Press, Wellesley, MA, 2007.

[105] Y.A. Pirogov and A.V. Tikhonravov. Resonance absorption of wave energy in asymmetrical multilayer structures. *Radioelektronika*, 21:15–20, 1978.

[106] J.D. Jackson. *Classical Electrodynamics.* Wiley, New York, 1999.

[107] S. A. Campbell. *Fabrication Engineering at the Micro- and Nanoscale.* Oxford University Press, USA, 2008.

[108] M. Laroche, R. Carminati, and J. J. Greffet. Coherent thermal antenna using a photonic crystal slab. *Phys. Rev. Lett.*, 96:123903, 2006.

[109] Jean-Jacques Greffet, Remi Carminati, Karl Joulain, Jean-Philippe Mulet, Stephane Mainguy, and Yong Chen. Coherent emission of light by thermal sources. *Nature*, 416:62–64, 2002.

[110] D. R. Smith, S. Schultz, N. Kroll, M. Sigalas K. M. Ho, and C. M. Soukoulis. Experimental and theoretical results for a two-dimensional metal photonic band-gap cavity. *Appl. Phys. Lett.*, 65(5):645–647, 1994.

[111] E. R. Brown and O. B. McMahon. Large electromagnetic stop bands in metallodielectric photonic crystals. *Appl. Phys. Lett.*, 67(15):2138–2140, 1995.

[112] David L. C. Chan, Marin Soljacic, and J. D. Joannopoulos. Thermal emission and design in one-dimensional periodic metallic photonic crystal slabs. *Phys. Rev. E*, 74:016609, 2006.

[113] David L. C. Chan, Marin Soljacic, and J. D. Joannopoulos. Thermal emission and design in 2d periodic metallic photonic crystal slabs. *Opt. Express*, 14(19):8785, 2006.

[114] Hitoshi Sai and Hiroo Yugami. Thermophotovoltaic generation with selective radiators based on tungsten surface gratings. *Appl. Phys. Lett.*, 85(16):3399–3401, 2004.

[115] Ivan Celanovic, Natalija Jovanovic, and John Kassakian. Two-dimensional tungsten photonic crystals as selective thermal emitters. *APL*, 92:193101, 2008.

[116] A. Heinzel, V. Boerner, A. Gombert, B. Blasi, V. Wittwer, and J. Luther. Radiation filters and emitters for the nir based on periodically structured metal surfaces. *Journal of Modern Optics*, 47(13):2399–2419, 2000.

[117] Hitoshi Sai, Yoshiaki Kanamori, Kazuhiro Hane, Hiroo Yugami, and Masafumi Yamaguchi. Numerical study on tungsten selective radiators with various micro/nano structures. *IEEE*, pages 762–765, 2005.

[118] Shawn-Yu Lin, J. G. Fleming, and I. El-Kady. Experimental observation of photonic-crystal emission near a photonic band edge. *Appl. Phys. Lett.*, 83(4):593–595, 2003.

[119] F. Reif. *Fundamentals of Statistical and Thermal Physics.* McGraw-Hill, 1965.

[120] H. H. Kolm. Solar-battery power source. Quarterly progress report, group 35, MIT Lincoln Laboratory, 1953.

[121] B. Wedlock. Thermo-photo-voltaic conversion. *Proc. IEEE*, 51:694–698, 1963.

[122] Michael W. Dashiell, John F. Beausang, Hassan Ehsani, G. J. Nichols, David M. Depoy, Lee R. Danielson, Phil Talamo, Kevin D. Rahner, Edward J. Brown, Steven R. Burger, Patrick M. Fourspring, William F. TopperJr., P. F. Baldasaro, Christine A. Wang, Robin K. Huang, Michael K. Connors, George W. Turner, Zane A. Shellenbarger, Gordon Taylor, Jizhong Li, Ramon Martinelli, Dmitry Donetski, Sergei Anikeev, Gregory L. Belenky, and Serge Luryi. Quaternary ingaassb thermophotovoltaic diodes. *IEEE Transactions on Electron. Devices*, 53(12):2879 –2891, 2006.

[123] Hermann A. Haus. *Waves and Fields in Optoelectronics.* Prentice-Hall, New Jersey, 1984.

[124] Ardavan F. Oskooi, David Roundy, Mihai Ibanescu, Peter Bermel, J. D. Joannopoulos, and Steven G. Johnson. Meep: A flexible free-software package for electromagnetic simulations by the fdtd method. *Computer Physics Communications*, 181:687–702, 2010.

[125] J. Bravo-Abad, F. J. Garcia-Vidal, and L. Martin-Moreno. Resonant transmission of light through finite chains of subwavelength holes in a metallic film. *Phys. Rev. Lett.*, 93:227401, 2004.

[126] C. Luo, A. Narayanaswamy, G. Chen, and J. D. Joannopoulos. Thermal radiation from photonic crystals: A direct calculation. *Phys. Rev. Lett.*, 93(21):213905, 2004.

[127] David L. C. Chan, Marin Soljacic, and J. D. Joannopoulos. Direct calculation of thermal emission for three-dimensionally periodic photonic crystal slabs. *Phys. Rev. E*, 74:036615, 2006.

[128] Shanhui Fan and J. D. Joannopoulos. Analysis of guided resonances in photonic crystal slabs. *Phys. Rev. B*, 65:235112, 2002.

[129] Shanhui Fan, Wonjoo Suh, and J. D. Joannopoulos. Temporal coupled-mode theory for the fano resonance in optical resonators. *J. Opt. Soc. Am. A*, 20(3):569–572, 2003.

[130] David L. C. Chan, Ivan Celanovic, J. D. Joannopoulos, and Marin Soljacic. Emulating one-dimensional resonant q-matching behavior in a two-dimensional system via fano resonances. *PRA*, 74:064901, 2006.

[131] Wonjoo Suh, Zheng Wang, and Shanhui Fan. Temporal coupled-mode theory and the presence of non-orthogonal modes in lossless multimode cavities. *IEEE J. Quantum Electron.*, 40(10):1511–1518, 2004.

[132] R.M. Swanson. A proposed thermophotovoltaic solar energy conversion system. *Proc. IEEE*, 67(3):446–447, 1979.

[133] W. Spirkl and H. Ries. Solar thermophotovoltaics: An assessment. *Journal of Applied Physics*, 57(9):4409–4414, 1985.

[134] Yong-Sung Kim, Shawn-Yu Lin, Allan S. P. Chang, Jae-Hwang Lee, and Kai-Ming Ho. Analysis of photon recycling using metallic photonic crystal. *J. Appl. Phys.*, 102:063107, 2007.

[135] J. J. Vos. Colorimetric and photometric properties of a 2° fundamental observer. *Color Res. & Appl.*, 3(3):125–128, 1978.

[136] Tatsunosuke Matsui, Amit Agrawal, Ajay Nahata, and Z. Valy Vardeny. Transmission resonances through aperiodic arrays of subwavelength aperatures. *Nature*, 446:517–521, 2007.

[137] J. Bravo-Abad, A. I. Fernandez-Dominguez, F. J. Garcia-Vidal, and L. Martin-Moreno. Theory of extraordinary transmission of light through quasiperiodic arrays of subwavelength holes. *Phys. Rev. Lett.*, 99:203905, 2007.